

Constructing meaningful FWI gradients for data from shaped DAS fibres

Matt Eaid, Scott Keating and Kris Innanen

ABSTRACT

Distributed acoustic sensing (DAS) has garnered significant interest as a seismic acquisition technology, especially in borehole deployments. Using non-invasive optical fibres, DAS can be placed in producing wells, abandoned wells, and horizontal wells during hydraulic fracture treatments. This powerful property of DAS fibres allows for the dual purposing of wells without shutting in production and offers a unique opportunity to densely sample the long wavelength transmission portion of the wavefield. A lingering question is how to best utilize DAS data to estimate reservoir properties. Elastic full waveform inversion is a robust means of estimating elastic subsurface parameters, but it is conventionally formulated to incorporate particle velocity data supplied by geophones. In contrast to geophones in conventional surveys which provide measurements of three orthogonal components of particle velocity, DAS supplies a single measurement of tangential strain or strain rate along the fibre. We reformulate the conventional least-squares FWI objective function to incorporate the strain data supplied by distributed acoustic sensing fibres. The method developed in this paper can incorporate strain data from straight and shaped DAS fibres, and because it utilizes the conventional FWI formulation is capable of inverting displacement data from geophones and DAS fibre simultaneously. We explore the effect that shaping DAS fibres has on the quality of parameter estimations from a toy model by comparing inversion results from a straight DAS fibre in a horizontal well and three helical fibres with varying wind rates. A simultaneous inversion of reflection geophone data and DAS data from horizontal well is examined and provides enhanced parameter estimations over either dataset alone. The simultaneous inversion is then tested on a portion of the Marmousi 2 model.

INTRODUCTION

Pioneered by Tarantola (1984, 1986, 1988) full waveform inversion (FWI) is a powerful method that provides an estimate of subsurface properties by iteratively minimizing the discrepancies between observed data from a seismic survey and modeled data from a postulated model. Most of the initial success in FWI focused on single parameter optimization in which acoustic wave physics and constant density were assumed. Wave propagation in the earth is generally more complex and requires multiple independent parameters for modeling. Multiparameter inversion frameworks allow for simultaneous and independent updates of multiple parameters. A form of multiparameter inversion, elastic full waveform inversion assumes an isotropic elastic medium whose characterization requires three independent elastic parameters. Elastic FWI seeks estimates of these three parameters, commonly p-wave velocity, s-wave velocity, and the density. While a theory for elastic FWI has existed for decades (Tarantola, 1986), its successful application to land datasets was hampered by the computational overhead and nonlinearity of multiparameter inversion. However, in recent years, strategies to reduce this nonlinearity in the objective function have lead to more success.

Conventionally, FWI minimizes the L_2 norm of the sample-by-sample difference between the observed and modeled data. If the observed and modeled data are out of phase by more than one half cycle then this type of objective function will erroneously update the model to match adjacent cycles of the observed and modeled data, a situation known as cycle skipping (Virieux and Operto, 2009). Many methods exist for the mitigation of cycle skipping, most of which focus on expanding the convexity of the objective function over some region (van Leeuwen and Mulder, 2010; Luo and Sava, 2011; Warner and Guasch, 2016; Metivier et al., 2018). However, the most successful methods for mitigating cycle skipping involve using data with low frequency information and ray paths containing long wavelength information about the model. Using the least-squares misfit function, cycle skipping can be avoided by starting the inversion at a sufficiently low frequency such that the modeled and observed data are within a half cycle. As the inversion progresses and the modeled data begins to agree with the observed data, the frequency band expands to improve the resolution of the inversion. Originally proposed by Bunks (1995) this method is known as the multiscale approach. For the multiscale approach to be effective the data must contain significant amplitude at a sufficiently low frequency so that the observed and modeled data are within a half cycle at that frequency. Typical geophones used for seismic acquisition have a natural corner frequency of approximately 10 Hz resulting in data that is rich in high frequency but poor in very low frequency content. Using the approach of Bunks (1995), success has been achieved on data from a model simulating land seismic data over a complex target, however, frequencies of 1.7 Hz were required to mitigate cycle skipping (Brossier et al., 2009). Frequencies this low may not always be available in geophone data. In order for inversions of this kind to be successful we require a means of recording these low frequencies.

Recent advances have created a novel technology for seismic data acquisition known as distributed acoustic sensing (DAS). Based on coherent, phase sensitive, optical time domain reflectometry (ϕ -OTDR) (Posey Jr. et al., 2000; Masoudi et al., 2013), DAS utilizes phase changes in Rayleigh backscattered light traversing an optical fibre to sense seismic strain. Since its adoption in the early part of this decade, distributed acoustic sensing has experienced rapid growth and development finding applications in microseismic monitoring (Karam et al., 2013; Karrenbach et al., 2018), vertical seismic profiling for reservoir monitoring (Mestayer et al., 2012; Daley et al., 2013; Mateeva et al., 2014), near surface monitoring (Dou et al., 2017), and time-lapse monitoring (Dou et al., 2016). From an FWI perspective, DAS technologies open the door for some interesting opportunities. Most encouraging, is the well documented ability of distributed acoustic sensing to provide very low frequency information, down to millihertz in some cases (Jin and Roy, 2017; Becker et al., 2018; Becker and Coleman, 2019). The access to low frequency data that DAS provides, could help bring elastic FWI to the reservoir. Additionally, DAS provides a low cost, noninvasive, alternative to geophones allowing them to be readily deployed in the borehole. In this configuration, they provide access to dense sampling of transmitted ray paths further increases the long wavelength information provided by DAS.

Due to the relatively high rigidity of the silica glass used in optical fibres, DAS is only sensitive to the components of the wavefield producing strain along the tangential direction of the fibre core (Kuvshinov, 2015). Distributed acoustic sensing is inherently a single component recording system, commonly described in the literature as having a broadside

insensitivity to strain (Kuvshinov, 2015). The sensitivity of the fibre can be improved by increasing the complexity of the fibre geometry so that it samples many tangent directions, a common choice of geometry being a helical fibre. In practice, to improve the signal to noise ratio the strain from many scatters over a spatial distance known as the gauge length is averaged (Dou et al., 2017). This means that a shaped fibre does not supply point measurements of the strain in a given tangential direction, but rather supplies the average of the strain in many tangential directions over the gauge length.

Three component geophones and DAS can be viewed as supplying complementary datasets. Distributed acoustic sensing holds the potential to supply the low frequency content that geophones cannot, whereas geophones provided a richer multicomponent dataset. Using the two together provides a more complete dataset that may improve inversions for subsurface parameters. In order to realize this goal a framework for the inversion of the strain data supplied by DAS must be developed. Early work in applying FWI to DAS was shown by Podgornova et al. (2017) and Egorov et al. (2018) with encouraging results. Most applications of FWI to DAS data have only considered a straight fibre in a VSP, and therefore only consider the z-component of displacement in the modeling of the DAS strain data. While this approach is correct for straight DAS fibre deployed in perfectly vertical wells it is not a flexible approach for deviated wells, horizontal wells, or shaped fibres. The goal of this paper is to develop a flexible means of computing the FWI gradient for DAS data, and exploring the role of shaped fibres in multiparameter inversion. Additionally, the complementary aspects of DAS and 3C geophones will be explored from an FWI perspective.

FORWARD MODELING OF DAS DATA

The forward modeling of distributed acoustic sensing data begins with a geometric model that at a minimum contains the position vector for the fibre axis, arc-length along the fibre, and the fibre tangent direction (Innanen, 2017; Eaid et al., 2018). The most important result of the geometric model is the transformation from an orthonormal basis in the field coordinates to an orthonormal basis in fibre coordinates containing the tangent (\mathbf{t}), normal (\mathbf{n}), and binormal (\mathbf{b}) unit vectors of the fibre (Pressley, 2012). It is along the tangent direction (\mathbf{t}) that the optical fibre senses the seismic strain.

The definition of an orthonormal basis for the fibre coordinates allows for the computation of the strain sensed by the fibre. To begin, the frequency domain 2D inhomogeneous isotropic elastic wave equation is solved using the system of equations presented by Pratt (1990),

$$\omega^2 \rho u_x + \frac{\partial}{\partial x} \left[\lambda \left(\frac{\partial u_x}{\partial x} + \frac{\partial u_z}{\partial z} \right) + 2\mu \frac{\partial u_x}{\partial x} \right] + \frac{\partial}{\partial z} \left[\mu \left(\frac{\partial u_z}{\partial x} + \frac{\partial u_x}{\partial z} \right) \right] + s_x = 0 \quad (1a)$$

$$\omega^2 \rho u_z + \frac{\partial}{\partial z} \left[\lambda \left(\frac{\partial u_x}{\partial x} + \frac{\partial u_z}{\partial z} \right) + 2\mu \frac{\partial u_z}{\partial z} \right] + \frac{\partial}{\partial x} \left[\mu \left(\frac{\partial u_z}{\partial x} + \frac{\partial u_x}{\partial z} \right) \right] + s_z = 0 \quad (1b)$$

where $u_x = u_x(x, z, \omega)$ and $u_z(x, z, \omega)$ are the frequency domain particle displacements in the x and z directions, s_x and s_z are the horizontal and vertical source components, ω is the angular frequency, $\lambda = \lambda(x, z)$ and $\mu = \mu(x, z)$ are the Lamé parameters, and $\rho = \rho(x, z)$ is the density. Solving equations (1a) and (1b) using the finite difference methods of Pratt (1990) provides the frequency domain wavefields for the horizontal and vertical displacements. The strain fields can then be computed using the definition of the strain tensor,

$$\epsilon_{ij} = \frac{1}{2} \left(\frac{\partial u_i}{\partial x_j} + \frac{\partial u_j}{\partial x_i} \right) \quad (2)$$

which in the 2D case can be solved using finite differences for ϵ_{xx} , ϵ_{xz} , and ϵ_{zz} . Careful analysis of equations (1a) and (1b), shows that the computation of the displacements involves strain terms like those contained in equation (2). The strain in equation (2) is therefore computed in an equivalent manner to the displacements in equations (1a) and (1b).

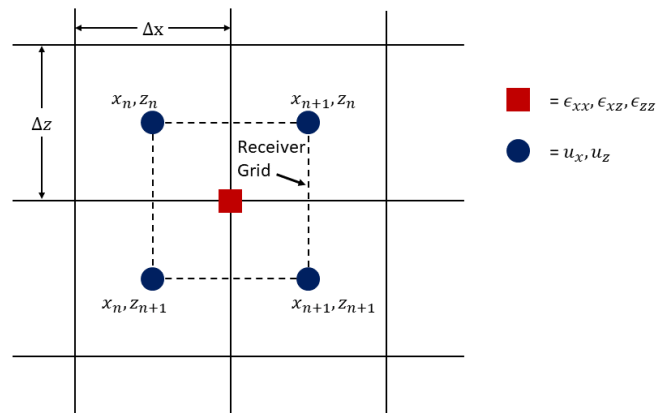


FIG. 1. Grid used for wavefield propagation and strain field computation. The blue circles represent grid points at which values of the displacement field are computed. The red square indicates the position of the receiver location used for strain field computation.

In practice, for greater stability, the strain fields in equation (2) are solved on a grid that is spatially staggered in x and z from the grid used for the displacement propagation as shown in figure 1. The blue circles are at grid points on the displacement grid and contain values of the horizontal and vertical components of displacement. Let $u_x(x_n, z_n)$ and $u_z(x_n, z_n)$ be the values of the x and z displacements in the northwest cell of figure 1, the strain values on the spatially staggered grid are then given by,

$$\epsilon_{xx} = \frac{1}{2} \left(\frac{u_x(x_{n+1}, z_{n+1}) - u_x(x_n, z_{n+1})}{\Delta x} + \frac{u_x(x_{n+1}, z_n) - u_x(x_n, z_n)}{\Delta x} \right) \quad (3a)$$

$$\epsilon_{zz} = \frac{1}{2} \left(\frac{u_z(x_{n+1}, z_{n+1}) - u_z(x_{n+1}, z_n)}{\Delta z} + \frac{u_z(x_n, z_{n+1}) - u_z(x_n, z_n)}{\Delta z} \right) \quad (3b)$$

$$\begin{aligned} \epsilon_{xz} = & \frac{1}{4} \left(\frac{u_x(x_{n+1}, z_{n+1}) - u_x(x_{n+1}, z_n)}{\Delta z} + \frac{u_x(x_n, z_{n+1}) - u_x(x_n, z_n)}{\Delta z} \right) \\ & + \frac{1}{4} \left(\frac{u_z(x_{n+1}, z_{n+1}) - u_z(x_n, z_{n+1})}{\Delta x} + \frac{u_z(x_{n+1}, z_n) - u_z(x_n, z_n)}{\Delta x} \right). \end{aligned} \quad (3c)$$

Fibre sensitivity

Once the strain field is computed it must be transformed from the coordinate system used in modeling into the orthonormal basis of the fibre through projection of the strain field onto the fibre. The projection of the strain tensor can be computed using the formula for the rotation of a rank 2 tensor (Krebes, 2019)

$$\epsilon_{tnb} = \mathbf{P} \epsilon_{xyz} \mathbf{P}^T \quad (4)$$

where ϵ_{xyz} is the strain tensor in Cartesian coordinates, ϵ_{tnb} is the strain tensor in the coordinates of the fibre, and \mathbf{P} is the rotation matrix taking the strain tensor from the modeling coordinate system to the fibre coordinate system. The matrix \mathbf{P} is the standard rotation matrix, formed through the projection of the Cartesian unit vectors ($\hat{\mathbf{1}}, \hat{\mathbf{2}}, \hat{\mathbf{3}}$) onto the fibre unit vectors ($\hat{\mathbf{t}}, \hat{\mathbf{n}}, \hat{\mathbf{b}}$) through the dot product,

$$\mathbf{P} = \begin{bmatrix} \hat{\mathbf{t}} \cdot \hat{\mathbf{1}} & \hat{\mathbf{t}} \cdot \hat{\mathbf{2}} & \hat{\mathbf{t}} \cdot \hat{\mathbf{3}} \\ \hat{\mathbf{n}} \cdot \hat{\mathbf{1}} & \hat{\mathbf{n}} \cdot \hat{\mathbf{2}} & \hat{\mathbf{n}} \cdot \hat{\mathbf{3}} \\ \hat{\mathbf{b}} \cdot \hat{\mathbf{1}} & \hat{\mathbf{b}} \cdot \hat{\mathbf{2}} & \hat{\mathbf{b}} \cdot \hat{\mathbf{3}} \end{bmatrix}. \quad (5)$$

Distributed acoustic sensing is only sensitive to the tangential (ϵ_{tt}) component of the fibre strain tensor (ϵ_{tnb}) in equation (4). Expanding equation (4) with the definition of the rotation matrix in equation (5) and extracting the ϵ_{tt} component yields the strain sensed by an arbitrary fibre geometry,

$$\epsilon_{tt} = (\hat{\mathbf{t}} \cdot \hat{\mathbf{1}})^2 \epsilon_{xx} + 2(\hat{\mathbf{t}} \cdot \hat{\mathbf{1}})(\hat{\mathbf{t}} \cdot \hat{\mathbf{2}}) \epsilon_{xy} + 2(\hat{\mathbf{t}} \cdot \hat{\mathbf{1}})(\hat{\mathbf{t}} \cdot \hat{\mathbf{3}}) \epsilon_{xz} + (\hat{\mathbf{t}} \cdot \hat{\mathbf{2}})^2 \epsilon_{yy} + 2(\hat{\mathbf{t}} \cdot \hat{\mathbf{2}})(\hat{\mathbf{t}} \cdot \hat{\mathbf{3}}) \epsilon_{yz} + (\hat{\mathbf{t}} \cdot \hat{\mathbf{3}})^2 \epsilon_{zz}. \quad (6)$$

In 2D wavefield simulations the components of strain with particle motion in the y -direction are zero, reducing equation (6) to,

$$\epsilon_{tt} = (\hat{\mathbf{t}} \cdot \hat{\mathbf{1}})^2 \epsilon_{xx} + 2(\hat{\mathbf{t}} \cdot \hat{\mathbf{1}})(\hat{\mathbf{t}} \cdot \hat{\mathbf{3}}) \epsilon_{xz} + (\hat{\mathbf{t}} \cdot \hat{\mathbf{3}})^2 \epsilon_{zz}. \quad (7)$$

Equation (7) shows that the strain sensed by the fibre is a weighted sum of the Cartesian components of the wavefield. The weights are geometry dependent and express the sensitivity of a given fibre geometry to each component of the Cartesian strain field.

Straight fibres in vertical wells are the most commonly deployed fibre geometry. In this case the tangent direction of the fibre is constant over the length of the fibre and only has a vertical component, resulting in a fibre geometry that is only sensitive to the vertical (ϵ_{zz}) component of strain. Clearly, fibres of this type are incapable of measuring a potentially large portion of the wavefield. Research has focused on shaping fibres in more complex geometric shapes to increase the quantity of sampled tangents, providing a more complete subset of the wavefield (Innanen, 2017; Ning and Sava, 2018).

The Gauge Length

In practice DAS systems utilize an unbalanced Mach-Zehnder interferometer (MZI) to delay the signal scattered from one portion of the fibre (Masoudi et al., 2013). To achieve this, one arm of the interferometer is made longer than the other so that the interference pattern is composed of the light backscattered from two separated portions of the fibre. The separation of the two scattering centers is directly related to the length of the delay fibre in the MZI, and is known as the gauge length. All of the strain perturbations in the fibre between the two scattering centers affect the phase of the light scattered from the second scattering center. The interference pattern is therefore in a sense a function of the average strain between the two scattering centers, giving the average strain over the gauge length. While gauge lengths have been reported down to one meter (Daley et al., 2013), commonly gauge lengths on the order of ten meters are used to enhance the signal-to-noise ratio.

Fibre Geometries

Fibres are attractive for their ability to be deployed in wells without disrupting the production from the well. Inversions could benefit from additional information provided from downhole fibre as opposed to surface geophones alone. In this paper we consider various fibre geometries deployed in horizontal wells and investigate the effect of the geometry on the inversion result.

Fibres are often shaped to enhance the sensitivity of the fibre to a larger portion of the wavefield. Most of the commonly proposed fibre shapes are wrapped around a central core in well-defined geometric shapes. Let $d\ell$ be a small increment of fibre, \hat{c}_{\parallel} be the direction tangent to the core, and \hat{c}_{\perp} be a direction normal to the fibre core. We assume that the geometric shape chosen for the fibre is periodic, and that the gauge length (L) is long enough to include an integer number of periods. The gauge length averaged strain sensed by the fibre is then,

$$\epsilon_{tt}(\ell) = \int_0^L \left((\hat{t}(\ell) \cdot \hat{c}_{\parallel})^2 \epsilon_{c_{\parallel}c_{\parallel}} + 2(\hat{t}(\ell) \cdot \hat{c}_{\parallel})(\hat{t}(\ell) \cdot \hat{c}_{\perp}) \epsilon_{c_{\parallel}c_{\perp}} + (\hat{t}(\ell) \cdot \hat{c}_{\perp})^2 \epsilon_{c_{\perp}c_{\perp}} \right) d\ell. \quad (8)$$

Assuming the wavelength is much larger than the gauge length, which is common at seismic wavelengths, then the wavefield is approximately constant within the gauge length. The projection of the shear strain in this coordinate system, $\epsilon_{c_{\parallel}c_{\perp}}$, onto the fibre tangent, $\hat{t}(\ell)$, is given by the second term of equation (8). Let this term be defined as,

$$\psi = 2\epsilon_{c_{\parallel}c_{\perp}} \int_0^L c'_{\parallel}(\ell) c'_{\perp}(\ell) d\ell. \quad (9)$$

where $c'_{\parallel}(\ell)$ is the projection of the core tangent onto the fibre, and $c'_{\perp}(\ell)$ is the projection of the core normal onto the fibre. Suppose the chosen fibre is symmetric in the sense that for each segment L_p^- to L_p^+ on which $c'_{\perp}(L_p^-) = c'_{\perp}(L_p^+) = c'_{\perp}(0)$ there exists a δ_p such that $L_p^- + \delta_p > 0$, $L_p^+ + \delta_p < L_p$, $c'_{\parallel}(\ell + \delta_p) = c'_{\parallel}(\ell)$, and $c'_{\perp}(\ell + \delta_p) = -c'_{\perp}(\ell)$, independent of the choice of coordinate system. In words, this definition of symmetry states that for every point on the fibre, ℓ , there exists a point, $\ell + \delta_p$, such that the direction of the projection of the fibre core onto the fibre tangent is preserved, and the projection of the normal to the fibre core onto the fibre tangent points in the opposite direction. Using this definition of symmetry in the integral of equation (9) results in

$$\psi = 2\epsilon_{c_{\parallel}c_{\perp}} \sum_p \int_{L_p^-}^{L_p^+} \left(c'_{\parallel}(\ell) c'_{\perp}(\ell) + c'_{\parallel}(\ell + \delta_p) c'_{\perp}(\ell + \delta_p) \right) d\ell \quad (10)$$

which reduces to,

$$\psi = 2\epsilon_{c_{\parallel}c_{\perp}} \sum_p \int_{L_p^-}^{L_p^+} c'_{\parallel}(\ell) \left(c'_{\perp}(\ell) - c'_{\perp}(\ell) \right) d\ell = 0. \quad (11)$$

Periodic fibres with this type of symmetry and gauge lengths much longer than the period are therefore insensitive to the $\epsilon_{c_{\parallel}c_{\perp}}$ component of strain. In the 2D experiments we consider, fibres of this type are insensitive to the ϵ_{xz} component of strain. This definition encompasses many commonly proposed fibre geometries including helical wound fibres, and chirped helical fibres in which the wind rate is allowed to ramp up and down over the period. Any fibre of this type is fully characterized by its ratio of sensitivity to ϵ_{xx} and ϵ_{zz} , given by the ratio of $(\hat{\mathbf{t}} \cdot \hat{\mathbf{1}})^2$ to $(\hat{\mathbf{t}} \cdot \hat{\mathbf{3}})^2$. Helical fibres can characterize any fibre of this type because any ratio $(\hat{\mathbf{t}} \cdot \hat{\mathbf{1}})^2 : (\hat{\mathbf{t}} \cdot \hat{\mathbf{3}})^2$ can be formed through careful consideration of the helix wind rate. In this paper the gauge length is implemented by taking the average of the sensitivity to ϵ_{xx} and ϵ_{zz} over each grid cell.

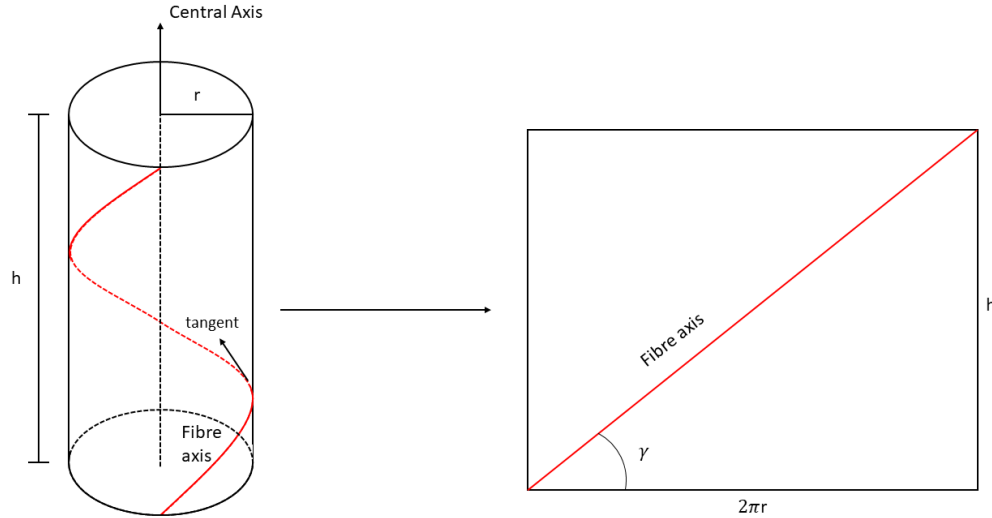


FIG. 2. One period of a helical fibre in red wrapped around a central axis. The cylinder can be unwrapped into a rectangle with dimensions of the circumference ($2\pi r$) and the cylinder height. The angle γ is referred to as the lead angle and describes the rate of the helix wind. Modified from Kuvshinov (2015).

Figure 2 shows the basic geometry for a helical wrapped fibre, where h is the distance advanced by the helix in one revolution, r is the radius of the helix, and the lead angle γ is given by $\gamma = \tan(h/2\pi r)$. Any periodic fibre that is symmetric according to the definition above can be characterized by a helical fibre with the appropriate sensitivity to ϵ_{xx} and ϵ_{zz} , controlled by the lead angle. This study compares the parameter estimations from helical DAS fibres of varying lead angles and a straight DAS fibre in horizontal wells. Varying the lead angle produces different sensitivity ratios, well a straight fibre in a horizontal well has only ϵ_{xx} sensitivity. Combining equations (7) and (8), a fibre whose core is oriented in the x -direction, has a ratio of ϵ_{xx} and ϵ_{zz} sensitivities given by

$$\frac{\epsilon_{xx}}{\epsilon_{zz}} = \frac{\int_0^L (\hat{\mathbf{t}}(\ell) \cdot \hat{\mathbf{1}})^2 d\ell}{\int_0^L (\hat{\mathbf{t}}(\ell) \cdot \hat{\mathbf{3}})^2 d\ell}. \quad (12)$$

For a helical fibre with lead angle γ whose central axis is in the x -direction (see figure 2), the expression in equation (12) becomes,

$$\frac{\int_0^L (\hat{\mathbf{t}}(\ell) \cdot \hat{\mathbf{1}})^2 d\ell}{\int_0^L (\hat{\mathbf{t}}(\ell) \cdot \hat{\mathbf{3}})^2 d\ell} = \frac{\sin^2 \gamma}{\cos^2 \gamma \langle \cos^2 \theta \rangle} = 2 \frac{\sin^2 \gamma}{\cos^2 \gamma} \quad (13)$$

where $\langle \cos^2 \theta \rangle = 1/2$ is the expectation of the z -component of the tangent direction as the helix winds about the central axis.

Fibres with a lead angle of $\gamma = \arctan(1/\sqrt{2})$, or approximately 35 degrees, represent a special case of a fibre equally sensitive to ϵ_{xx} and ϵ_{zz} . Careful review of equation (7) shows

that when this criteria is met the strain response is given by,

$$\epsilon_{tt} = \epsilon_{xx} + \epsilon_{zz} = \nabla \cdot \mathbf{u}. \quad (14)$$

While fibres of this type benefit from data sufficiency, equation (14) shows they are shear wave blind. Fibres of this type are wave mode discriminatory, sensing only the compressional component of wave motion. Later we explore the effect of shear blindness on the inversion results of v_p , v_s , and ρ . Figure 3 (a) shows a fibre of this type, while figures 3 (c)-(d) show the sensitivity in blue and the gauge length averaged sensitivity in red.

We also consider three additional fibre geometries, a straight fibre, a 4:1 fibre, and a 1:4 fibre, where the ratios indicate the relative sensitivity of a fibre in $\epsilon_{xx} : \epsilon_{zz}$. Straight fibres are commonly deployed, and it is important here to understand their efficacy in inversion. While straight fibres are data deficient, sensing only one of the three 2D components of strain, they benefit from having absolute certainty about what portion of the wavefield they measured. Horizontal straight fibres only record ϵ_{xx} , and will only back propagate ϵ_{xx} components in FWI. Based on the survey geometry, the equal sensitivity helical fibre discussed above might record more ϵ_{zz} but will back propagate equal weightings of ϵ_{xx} and ϵ_{zz} potentially creating a mismatch between forward and back propagated wavefields. The next geometry we consider is a fibre with a gentle wind such that its response is dominated by ϵ_{xx} . For this we choose a fibre with a 54.7 degree degree wind so that it is four times more sensitive to ϵ_{xx} than it is to ϵ_{zz} . This case provides insight into how the inversion is effected by adding additional data sensitivity. We also consider the opposite case of a fibre with a lead angle of 19.5 degrees being four times more sensitive to ϵ_{zz} than it is to ϵ_{xx} . For horizontal fibres, assuming small offsets, the majority of the wave propagation is in the vertical direction, and the 19.5 degree fibre should have the greatest sensitivity to the propagating wavefield. Later we explore how the choice of wrapping angles effects the successful estimation elastic subsurface parameters.

It is important to note that every fibre meeting the symmetry criteria above is insensitive to shear strain (ϵ_{xz}) components, restricting the data they can record. Realistic fibre geometries can be constructed that violate this definition of symmetry allowing for enhanced strain sensitivity, an example of which is shown in figure 4. This fibre consists of segments of four and half winds of a 19.25 degree helical fibre connected by a half wind of 59.5 degree helical winds. This geometry is specifically designed to violate the definition of symmetry above and produces a fibre that has a 2:1:2 sensitivity ratio of $\epsilon_{xx} : \epsilon_{xz} : \epsilon_{zz}$. This example shows that asymmetric fibres can be designed to have significant sensitivity to ϵ_{xz} , increasing the portion of the wavefield that is recorded. Geometries of this type will also be tested for their efficacy in FWI for parameter estimation.

Scattering Radiation Patterns

Radiation patterns provide information about the wavefields scattered by a model parameter through the partial derivative of the wavefield with respect to that model parameter. The effect perturbing a model parameter has on the wavefield can be examined through analysis of scattering radiation patterns, computed from the partial derivative wavefields

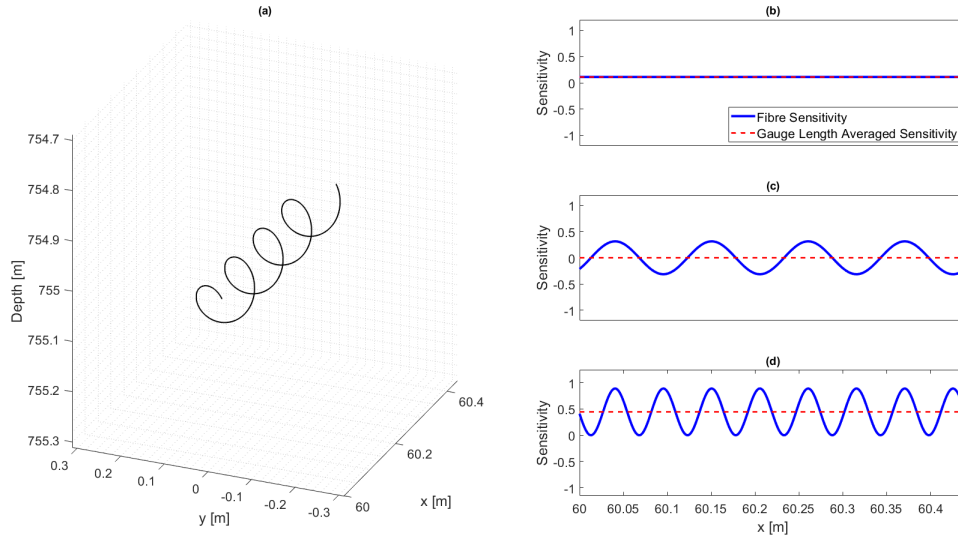


FIG. 3. Effect of gauge length on the sensitivities from 35 degree helix. (a) Helical fibre in black. Sensitivities of the helical in blue and the average sensitivity over the gauge length in red to the ϵ_{xx} component of the strain field (b), ϵ_{xz} (c), and ϵ_{zz} (d).

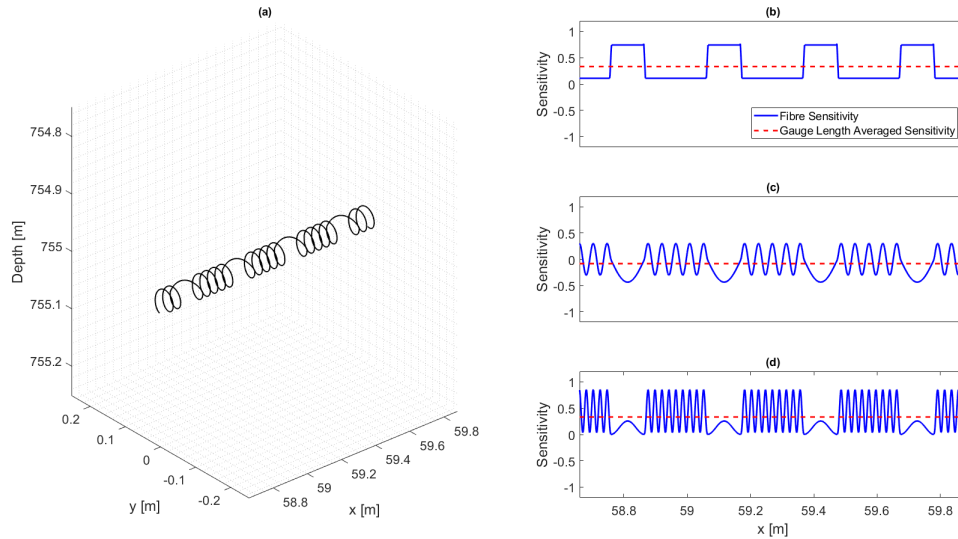


FIG. 4. Fibre sensitivities for an asymmetric fibre constructed from segments of a 19.25 degree helix connected by half periods of a 59.5 degree helix. Fibre geometry (a), sensitivities of the helical in blue and the average sensitivity over the gauge length in red to the ϵ_{xx} component of the strain field (b), ϵ_{xz} (c), and ϵ_{zz} (d).

with respect to that model parameter. They are an important tool for understanding the effect perturbing a certain model parameter has on the scattered wavefield at varying scattering angles. Numerically they are computed by taking the difference of the wavefields in a reference medium and a perturbed medium.

Scattering radiation patterns provide insight into the resolution of model parameters at different scattering angles. Large amplitudes at a given scattering angle indicate the

model parameter has a large effect on the wavefield at that angle, while small amplitudes indicate the model parameter does not affect the wavefield for those scattering angles. If two model parameters produce similar scattering patterns over the same range of scattering angles, then the two parameters have a similar effect on scattered wavefields and are hard to distinguish from each other at those angles. This results in an FWI phenomenon known as cross-talk in which data residuals caused by one parameter are attributed with another. When this occurs a parameter update can occur in the incorrect variable at locations of perturbations in the parameter causing the scattering.

Figure 5 shows scattering radiation patterns of displacement wavefields for perturbations in v_p , v_s , and ρ . The top row shows the z-component of the radiation patterns for v_p , v_s and ρ in (a)-(c) while the bottom row shows the x-component of the radiation patterns for v_p , v_s and ρ in (d)-(f). These radiation patterns show a snapshot of the displacement wavefield scattering from a model perturbation at the location of the green dot at a given time. In the radiation patterns for the z-component of displacement we can imagine a 1C, vertically oriented, geophone located at each grid point. The scattering radiation patterns then shows the displacement each of these geophones would sense. Similarly, the scattering radiation pattern for the x-displacement shows the response of 1C geophones oriented horizontally.

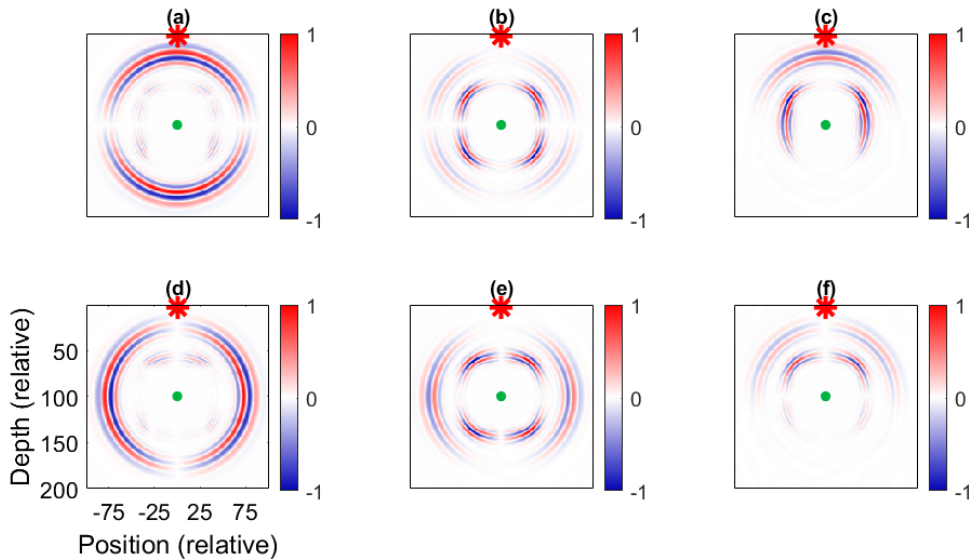


FIG. 5. Displacement scattering radiation patterns for v_p , v_s and ρ . Panels (a)-(c) show the z-component scattering radiation patterns for perturbations in v_p , v_s , and ρ respectively. Panels (d)-(f) show the x-component scattering radiation patterns for perturbations in v_p , v_s , and ρ respectively. The red star indicates the source location for wavefield modeling while the green circle indicates the location of the model perturbation.

Strain radiation patterns for v_p , v_s and ρ can be computed by applying the spatial derivatives in equation (2) to the displacement radiation patterns in figure 5. The strain radiation patterns calculated in this way are shown in figure 6. The top row shows the ϵ_{xx} radiation patterns for v_p , v_s , and ρ in panels (a)-(c). Panels (d)-(f) show the same for the ϵ_{xz} components, and panels (h)-(i) for the ϵ_{zz} components.

We can also construct fibre strain radiation patterns to understand the sensitivity of a

given fibre geometry to the strain radiation patterns. To interpret the fibre strain radiation patterns we begin by imagining a sheet that is placed over the the radiation patterns in figure 6. Every point in this sheet contains a small segment of straight or helical DAS fibre with a wind that produces the correct ratio of sensitivity to ϵ_{xx} and ϵ_{zz} . The fibre strain radiation pattern at each point then shows the response of a fibre segment at that point to a wavefield generated by a perturbation in the model parameter of interest. They provide insight into the sensitivity of a given fibre geometry to each model parameter at varying scattering angles and are an important tool in understanding the inversion results in the numerical examples below.

Using equation (7), the fibre strain radiation patterns for a given model parameter can be calculated through the weighted sum of the ϵ_{xx} , ϵ_{xz} , and ϵ_{zz} strain radiation patterns for that model parameter, where the weights are dependent on the fibre geometry. For example, the v_p fibre strain radiation pattern for a fibre with equal sensitivity to ϵ_{xx} and ϵ_{zz} can be computed by summing the radiation patterns in figure 6(a) and 6(g) with equal weights on both panels. The fibre strain radiation patterns for straight, 4:1, 1:1, and 1:4 fibres in a horizontal well are shown in figure 7 (a)-(c), (d)-(f), (g)-(i), and (j)-(l) respectively, where the ratios indicate the relative fibre sensitivity to ϵ_{xx} and ϵ_{zz} .

Figure 7 highlights some important characteristics of the scattering patterns for the four symmetric fibre geometries selected in this paper. Figure 7 (g)-(i) represents the scattering radiation patterns for a fibre that has equal sensitivity to ϵ_{xx} and ϵ_{zz} . Earlier in the discussion we indicated this fibre geometry was only sensitive to the dilatational component of the wavefield, and was therefore blind to shear waves. Examining the radiation patterns in figure 7 (g)-(i) confirms this, as the scattering patterns for all three variables lack shear modes. Additionally, the v_p and v_s scattering patterns are similar over a large range of scattering angles, indicating they may cross talk into each other. Figure 7 (a)-(c) shows the radiation patterns for a straight fibre while figure 7 (d)-(f) shows the radiation patterns for 4:1 fibre. Comparing these panels indicates that adding a small amount of information about ϵ_{zz} by gently winding the fibre does not significantly alter the radiation patterns, except at near normal reflection and transmission angles. This tells us that we might expect a straight fibre to produce comparable inversion results to a gently wound fibre. The radiation patterns for the 1:4 fibre in figure 7 (j)-(l) show that a tightly wound fibre provides significantly different information than the straight or 4:1 fibres. First it is more sensitive to vertical components of p-wave scattering, indicating that it might perform better than the other fibres when inverting data with the majority of wave motion in the vertical direction. Second, figure 7(j) and (k) indicate a strong decoupling between p-wave and s-wave scattering in v_p and v_s due to the lack of similarity in panels (j) and (k). Fibres of this type may be more immune to v_p and v_s cross talk than the other fibre geometries discussed here. All of the fibres presented here lack significant sensitivity to density perturbations at transmission scattering angles indicating that fibres deployed in horizontal wells may struggle with inverting for density. Although fibres are not commonly deployed for use in reflection seismology, the radiation patterns in figure 7 indicate tightly wound fibres would have the greatest sensitivity to wavefields at reflection scattering angles.

We will also consider the asymmetric fibre geometry shown in figure 4 (a), which has a sensitivity ratio of $2\epsilon_{xx} : \epsilon_{xz} : 2\epsilon_{zz}$. The radiation patterns for a fibre of this type are shown

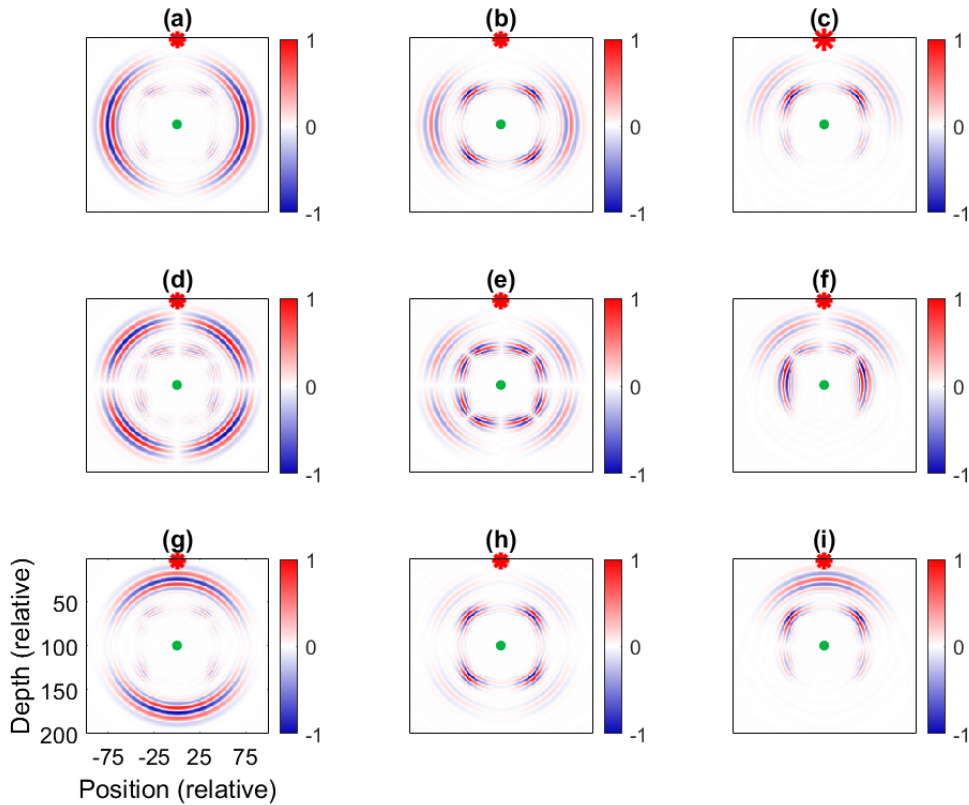


FIG. 6. Strain scattering radiation patterns for v_p , v_s and ρ . Panels (a)-(c) show the ϵ_{xx} -component scattering radiation patterns for perturbations in v_p , v_s , and ρ respectively. Panels (d)-(f) show the ϵ_{xz} -component scattering radiation patterns for perturbations in v_p , v_s , and ρ respectively. Panels (g)-(i) show the ϵ_{zz} -component scattering radiation patterns for perturbations in v_p , v_s , and ρ respectively. The red star indicates the source location for wavefield modeling while the green circle indicates the location of the model perturbation.

in figure 8.

These radiation patterns reveal important properties of asymmetric fibres. In this case the sign on the ϵ_{xz} sensitivity is negative, producing an asymmetry and preferred direction in the radiation patterns. Additionally, fibres of this type provide near-complete sensitivity of both p and s-wave modes as shown by the large amplitudes at nearly all scattering angles for p-wave energy in (a) and s-wave energy in (b). This fibre has better sensitivity to density perturbations over the helical fibres. The impact of this one the inversion quality will be assessed with examples later in the paper.

FULL WAVEFORM INVERSION

We begin the discussion of full waveform inversion by reviewing conventional least squares FWI of 3C geophone data, as it is closely tied to our method. The objective function in least squares FWI is formulated to minimize the L_2 norm of the difference between observed data, and modeled data from a predicted model,

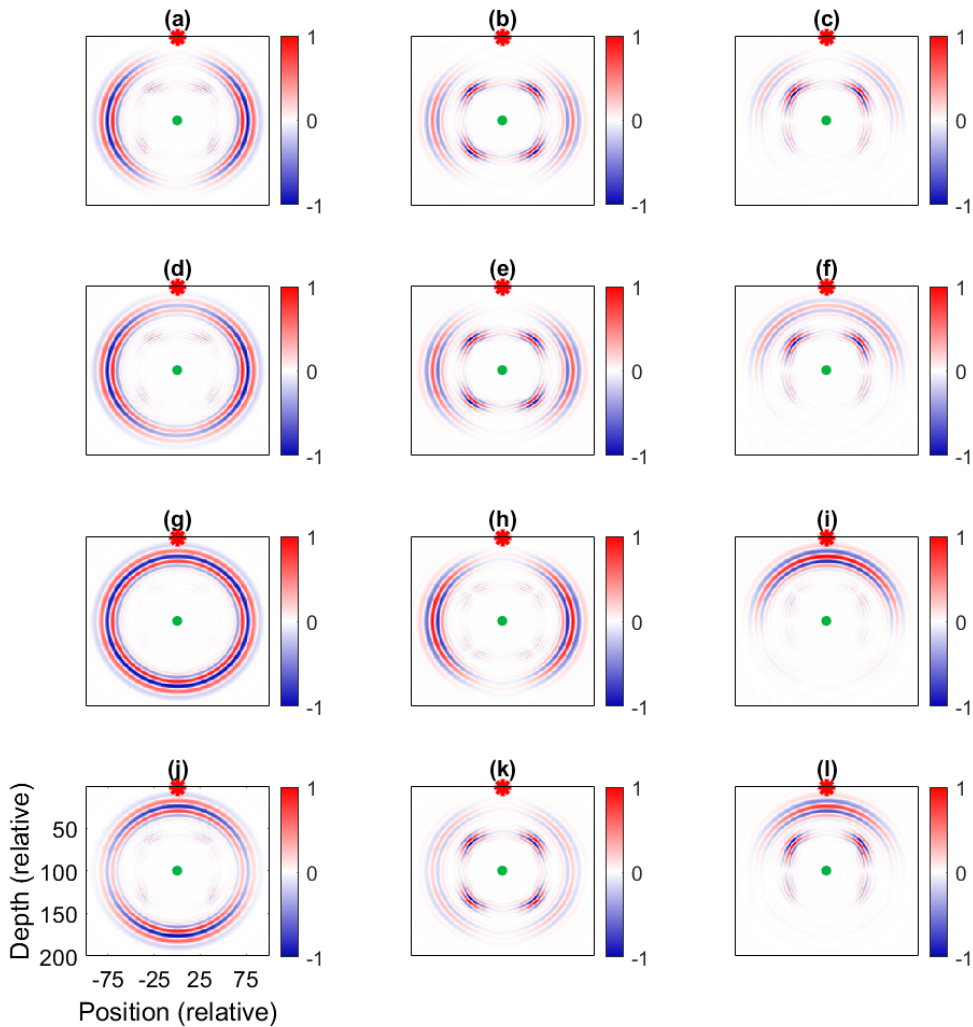


FIG. 7. Strain scattering radiation patterns for v_p , v_s and ρ . Panels (a)-(c) show the scattering radiation patterns for a straight fibre, for perturbations in v_p , v_s , and ρ respectively. Panels (d)-(f) show the scattering radiation patterns for a 4:1 fibre, for perturbations in v_p , v_s , and ρ respectively. Panels (g)-(i) show the scattering radiation patterns for a 1:1 fibre, for perturbations in v_p , v_s , and ρ respectively. Panels (j)-(l) show the scattering radiation patterns for a 1:4 fibre, for perturbations in v_p , v_s , and ρ respectively. The red star indicates the source location for wavefield modeling while the green circle indicates the location of the model perturbation.

$$\phi = \frac{1}{2} \|\mathbf{R}\mathbf{u} - \mathbf{d}\|_2^2 \quad (15)$$

where \mathbf{R} is a receiver matrix, which in the case of geophones samples the wavefield at the receiver positions, \mathbf{u} is the modeled wavefield from equations (1a) and (1b), and \mathbf{d} is the observed data. Equation (15) can be written as a constrained optimization problem in the following way:

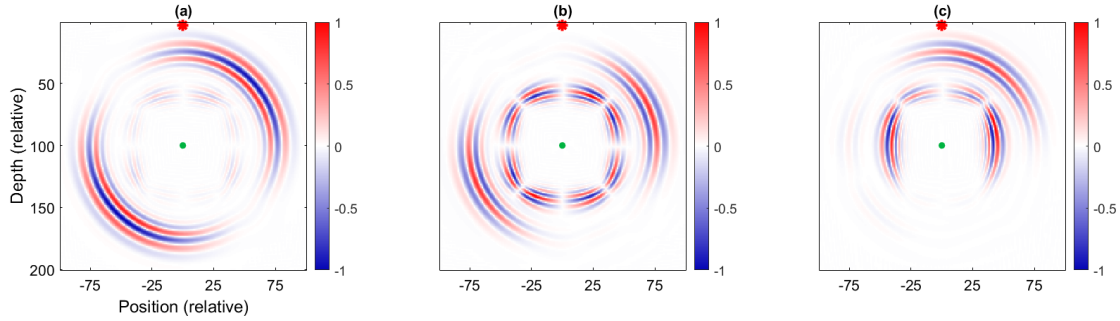


FIG. 8. Strain scattering radiation patterns for v_p , v_s and ρ in (a)-(c) respectively for a $2\epsilon_{xx} : \epsilon_{xz} : 2\epsilon_{zz}$ asymmetric fibre. The red star indicates the source location for wavefield modeling while the green circle indicates the location of the model perturbation.

$$\min_{\mathbf{m}} \frac{1}{2} \|\mathbf{R}\mathbf{u} - \mathbf{d}\|_2^2 \quad \text{subject to} \quad \mathbf{S}\mathbf{u} = \mathbf{f} \quad (16)$$

where \mathbf{S} is the wave equation operator, \mathbf{m} are the model parameters, and \mathbf{f} is the source function. The model parameters used in this paper are the p-wave square slowness ($1/v_p^2$), s-wave squared slowness ($1/v_s^2$), and density (ρ). Equation (16) can be solved using the method of Lagrange multipliers with the Lagrangian,

$$\mathcal{L}(\mathbf{m}, \mathbf{u}, \lambda) = \frac{1}{2} \|\mathbf{R}\mathbf{u} - \mathbf{d}\|_2^2 + \langle \mathbf{S}(\mathbf{m})\mathbf{u} - \mathbf{f}, \lambda \rangle \quad (17)$$

where $\langle \dots \rangle$ represents the inner product and λ is the Lagrange multiplier hereafter referred to as the adjoint variable.

The Lagrangian in equation (17) can be solved for the gradient of the objective function ϕ with respect to the model parameters \mathbf{m} using the adjoint state method. Metivier et al. (2013) give the gradient from the adjoint state method as,

$$\frac{\partial \phi}{\partial \mathbf{m}} = \left\langle \frac{\partial \mathbf{S}}{\partial \mathbf{m}} \mathbf{u}, \lambda \right\rangle \quad (18)$$

where the adjoint variable λ can be computed from,

$$\mathbf{S}^\dagger \lambda = \mathbf{R}^T (\mathbf{R}\mathbf{u} - \mathbf{d}). \quad (19)$$

The gradient in equation (18) can be seen to be formed by the correlation of a forward propagated wavefield and a back propagated adjoint wavefield.

Newton optimization methods find descent directions by solving the system of equations,

$$\mathbf{H}\Delta\mathbf{m} = -\mathbf{g} \quad (20)$$

where \mathbf{g} is the gradient of equation (18), $\Delta\mathbf{m}$ is the model update, and \mathbf{H} is the Hessian matrix of second derivatives. For typical seismic waveform inversion, the Hessian is too large to directly compute. Instead approximations to the Hessian are computed, sacrificing per iteration accuracy, but improving efficiency. In this paper the truncated Gauss-Newton method (TGN) is used to solve for the model updates, where the Hessian is iteratively approximated in an inner loop using the Broyden-Fletcher-Goldfarb-Shanno (BFGS) algorithm. A detailed discussion of TGN, and BFGS algorithms are provided in (Nocedal and Wright, 2006). Let \mathbf{B}_k be the approximate Hessian computed from the BFGS algorithm, α_k the step length at the current iteration found through line search algorithms, and $\nabla\phi(\mathbf{m}_k)$ the gradient at the current iteration. The model update is then given by,

$$\mathbf{m}_{k+1} = \mathbf{m}_k + \alpha_k \mathbf{B}_k^{-1} \nabla\phi(\mathbf{m}_k). \quad (21)$$

Inverting fibre strain data

Inverting DAS data requires an objective function that is a measure of the residual between modeled and observed fibre strain data. In the development of FWI for 3C geophone data the matrix \mathbf{R} samples the displacement wavefield at the locations of the receivers. However, it is important to note that no assumptions were made about the form of \mathbf{R} in the previous discussion. If an appropriate form of this matrix can be developed, such that the matrix-vector product $\mathbf{R}\mathbf{u}$ produces the fibre strain data, then equation (15) is a viable objective function for DAS data. In this paper, \mathbf{R} computes the Cartesian strain at the receiver locations using equations (3a)-(3c), projects these strains onto the fibre coordinates using equation (7), and invokes the gauge length by computing the average of the sensitivities in equation (7) over the length of fibre in the cell containing the receiver. Each point on the receiver grid which contains a receiver results in one data measurement of the fibre strain, as shown in figure 9. In the field, DAS fibres have dense trace spacing, on the order of less than one meter. At each trace, a measure of the average strain over a gauge length centered on that trace is recorded. To match field conditions our implementation should more correctly compute the strain data in each cell through the average of many measurements with overlap between adjacent cells. However, if the wavefield is approximately constant over a grid cell, which is true at seismic frequencies, then these extra measurements are highly redundant, so we neglect their consideration here. Figure 9 shows a representation of the matrix equation required to compute the fibre strain,

The receiver matrix also appears in the gradient through the back propagated adjoint wavefield. The correct formulation of matrix \mathbf{R} to compute fibre strain data, then also provides the gradient required for FWI of DAS fibre data. The BFGS algorithm uses the difference between gradients at the current and previous iteration to approximate the Hessian, and therefore also relies on the receiver matrix. Through proper handling of the receiver matrix to compute fibre strain data from the displacement wavefield, standard algorithms for FWI with 3C geophones can be used to invert DAS data. The approach presented here is readily adaptable to many FWI algorithms already in service. A powerful result

$$\begin{array}{ccc}
 \begin{bmatrix} \epsilon_{tt}^1 \\ \epsilon_{tt}^2 \\ \epsilon_{tt}^3 \\ \epsilon_{tt}^4 \\ \vdots \\ \epsilon_{tt}^{N_R-1} \\ \epsilon_{tt}^{N_R} \end{bmatrix} & = & \begin{bmatrix} R \\ \end{bmatrix} \\
 (N_R \times 1) & & (N_R \times 2N_g) \\
 & & \begin{bmatrix} u_{m_x}^1 \\ u_{m_z}^1 \\ u_{m_x}^2 \\ u_{m_z}^2 \\ \vdots \\ u_{m_x}^{N_g} \\ u_{m_z}^{N_g} \end{bmatrix} \\
 & & (2N_g \times 1)
 \end{array}$$

FIG. 9. Structural representation of the matrix equations required for the computation of fibre data.

of this method is that a receiver matrix may also be developed to simultaneously invert both geophone and fibre data. A portion of \mathbf{R} can be formulated to sample the displacement wavefield at the locations of the geophones, while another portion can be formulated to compute the fibre strain at the locations of the DAS fibre, as shown in figure 10. Formulations of this kind can be used to explore complementary geometries. Geophones are better suited for reflection experiments, while DAS fibres can be more readily deployed in horizontal wells. By formulating \mathbf{R} to handle surface geophones and buried DAS fibres we can explore the improvement in inversion results over reflection experiments alone. A structural representation of this formulation is shown in figure 10,

$$\begin{array}{ccc}
 \begin{bmatrix} d_{m_x}^1 \\ d_{m_z}^1 \\ d_{m_x}^2 \\ d_{m_z}^2 \\ \vdots \\ d_{m_x}^{N_{Rx}} \\ d_{m_z}^{N_{Rz}} \\ \hline \epsilon_{tt}^1 \\ \epsilon_{tt}^2 \\ \epsilon_{tt}^3 \\ \epsilon_{tt}^4 \\ \vdots \\ \epsilon_{tt}^{N_R-1} \\ \epsilon_{tt}^{N_R} \end{bmatrix} & = & \begin{bmatrix} R_{GEO} \\ \hline R_{DAS} \end{bmatrix} \\
 (N_R \times 1) & & (N_R \times 2N_g) \\
 & & \begin{bmatrix} u_{m_x}^1 \\ u_{m_z}^1 \\ u_{m_x}^2 \\ u_{m_z}^2 \\ \vdots \\ u_{m_x}^{N_g} \\ u_{m_z}^{N_g} \end{bmatrix} \\
 & & (2N_g \times 1)
 \end{array}$$

FIG. 10. Structural representation of the matrix equations required for simultaneous computation of geophone and fibre data.

SYNTHETIC EXAMPLE 1: THE ROLE OF THE LEAD ANGLE IN FIBRE INVERSIONS

To understand the effect that the lead angle has on inversion from shaped fibre data, and gain insight into the uplift provided by the simultaneous inversion of geophone and fibre data we begin by examining the inversion results from a toy model specifically designed to highlight the challenges associated with cross talk and parameter resolution. The true models for p-wave velocity (v_p), s-wave velocity (v_s), and density (ρ) are shown in figure 11 (a)-(c) respectively. This model is designed so that v_p , v_s , and ρ are spatially separated so that challenges arising from cross talk are evident. The anomalies are also localized to investigate parameter resolution. The starting models are constant with $v_p = 3000$ m/s, $v_s = 1800$ m/s, and $\rho = 1400$ kg/m³.

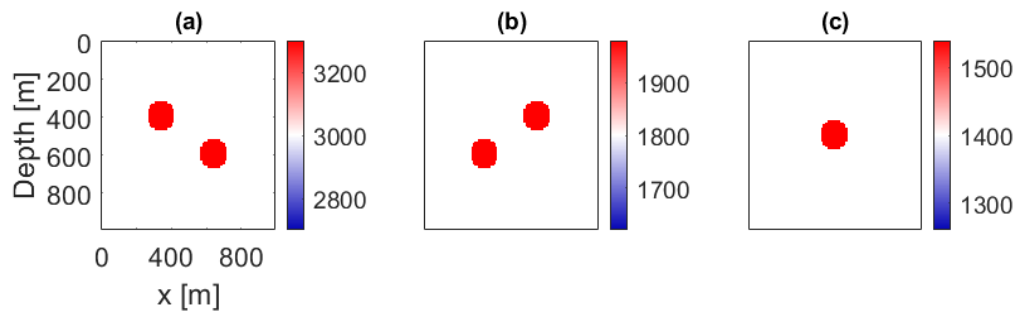


FIG. 11. Toy model used to test the effect of lead angle on fibre inversions. (a) P-wave velocity, v_p (m/s), (b) S-wave velocity, v_s (m/s), and (c) Density ρ (kg/m³).

Thirty-three explosive sources spaced 30 meters are used for modeling at a depth of 30 meters. The first source is 20 meters from the left edge of the model, and the last is 20 meters from right edge. Inversions are computed for straight, 4:1, 1:1, and 1:4 fibres oriented in the x-direction in a horizontal well at a depth of 750 meters. The trace spacing along the fibre for all four fibres is equal to the grid size of 10 meters. A multiscale Truncated Gauss-Newton optimization is used with one TGN iteration per frequency band. Ten frequency bands are used with eight equally spaced frequencies per band. The maximum frequency of each band increases by 2 Hz as the inversion proceeds where the first band contained frequencies from 1-2 Hz and the final band contained frequencies from 1-20 Hz. The Hessian is approximated using 20 inner loop iterations of BFGS. Figure 12 shows the inversion results for v_p in column 1, v_s in column 2 and density in column 3, for the straight (a)-(c), 4:1 (d)-(f), 1:1 (g)-(i), and 1:4 (m)-(l) fibres.

Figures 12 (a)-(c) and (d)-(f) show the inversion results for a horizontal straight fibre, and a helical fibre having four times more sensitivity to ϵ_{xx} than to ϵ_{zz} . The inversion results for all three parameters do contain subtle differences, but overall match each other well. This suggests that wrapping a fibre with a lead angle such that the same overall tangential direction is preserved, does not provide significant uplift from a straight fibre inversion. This result can be explained by comparing the fibre strain radiation patterns in figure 7 (a)-(c) and (d)-(f). Comparing these two radiation patterns shows that wrapping the fibre such that it is four times more sensitive to ϵ_{xx} as it is to ϵ_{zz} does not greatly alter the sensitivity of the fibre to the wavefield for any of the three parameters except at near normal transmission angles. Both fibres maintain similar tangential directions, and provide similar information

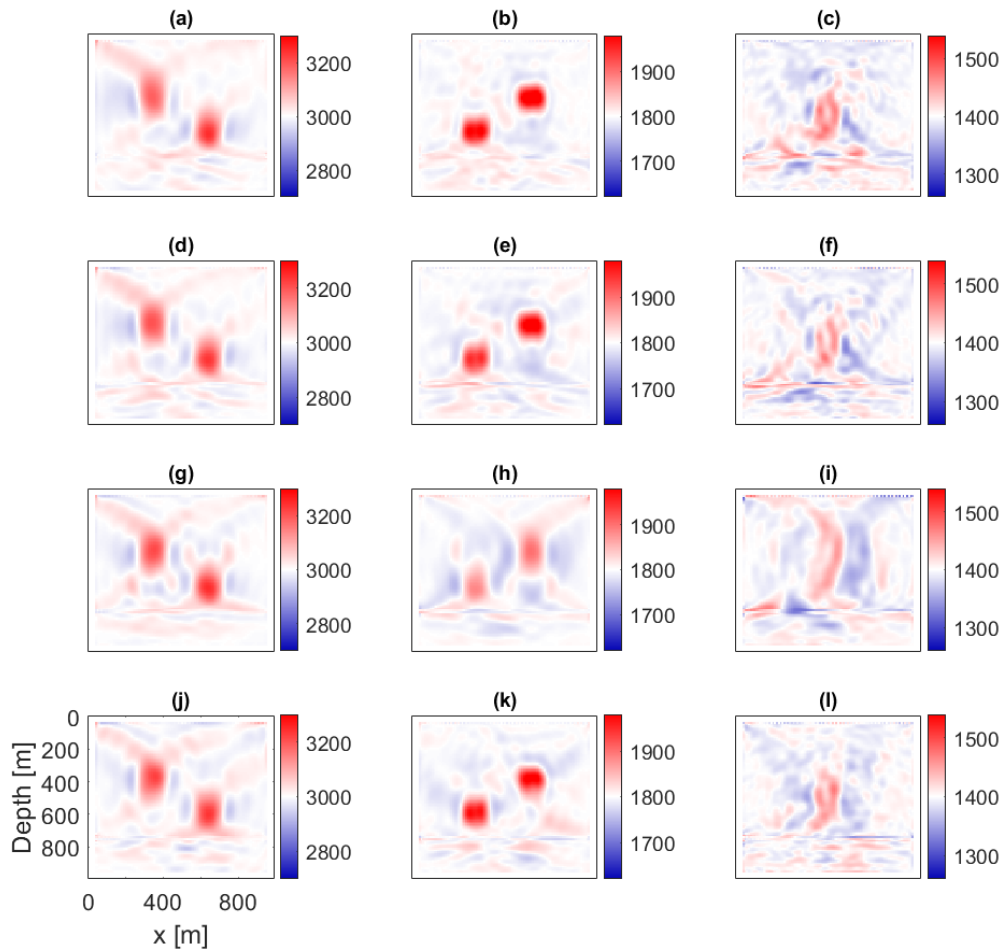


FIG. 12. FWI results for the four fibre types tested in this study. Inversion results for v_p (column 1), v_s (column 2), and ρ (column 3) for a straight fibre (a)-(c), 4:1 helical fibre (d)-(f), 1:1 helical fibre (g)-(i), and a 1:4 helical fibre (j)-(l).

for parameter estimation.

The inversion results for the 1:1 fibre are shown in figure 12 (g)-(i). The inversion results for v_p are comparable to the other three fibres, but the inversion result for v_s has poorer resolution and does not capture the amplitude of the anomalies as well as the other fibres. Although the inversion result for density from all four fibres are poor due to the lack of sensitivity to density at transmission angles, the inverted result for density from the 1:1 fibre has the poorest resolution. From previous discussion and analysis of the radiation patterns in figure 7 (g)-(i), this type of fibre measures the dilation of the wavefield and is blind to shear waves having a detrimental effect on the inversion of v_s and ρ . For the other three geometries, most of the information about density anomalies at transmission angles is provided by the shear wave. Because the 1:1 fibre lacks sensitivity to the transmitted shear wave, it lacks the information required for estimation of the density anomaly. The v_s radiation pattern completely overlays the v_p radiation pattern, resulting in challenges with resolving changes in the wavefield due to v_s anomalies. Fibres of this type most likely

obtain information about v_s and ρ from transmission AVO effects. The 1:1 fibre is able to resolve v_p well because it has perfect sensitivity to the changes in the wavefield caused by v_p at all scattering angles.

The inversion results for the 1:4 fibre, which is four times more sensitive to ϵ_{zz} than ϵ_{xx} are shown in figure 12 (j)-(l). The results for this fibre type are similar to those obtained using the straight and 4:1 fibre. This result is somewhat unexpected. The survey geometry produces wavefields that mostly propagate in the vertical direction. The 1:4 fibre is the most sensitive wavefields of this type as confirmed by the radiation patterns in figure 7 (j)-(l). These radiation patterns also indicate a better decoupling between the p and s-wavefields when comparing the scattering from v_p and v_s . This should reduce cross talk concerns, and allow for better resolution of both parameters. The density radiation pattern also shows that the 1:4 fibre has the best sensitivity to density anomalies at transmission angles, however, it is not significantly better, and the inversion for density is of similar quality. The similar quality in inversion results between the 1:4 and 4:1 fibres could be explained by a lack of noise in data use for the inversion. Without noise the 4:1 fibre provides small amplitude data at broadside angles that would typically be buried in noise in the field. In an inversion with noisy data, the 1:4 fibre will provide better data quality than the 4:1 fibre. It is also possible that the inversion for the 1:4 fibre converges faster and plateaus sooner, and the inversion from the 4:1 fibre obtains similar quality after more inversions. Both of these ideas will be tested in future work.

With the quality of the inversion result from DAS fibre, it was important to compare them to those from geophone data. Data from geophones with a spacing of 10 meters placed at the top of the model was inverted, the results of which are shown in figure 13 (a)-(c). The inversion results from the buried 1:4 fibre are repeated in figure 13 (d)-(f). Using a setup similar to that of figure 10, data from the surface geophones and buried fibre were simultaneously inverted, the results for which are shown in figure 13 (g)-(i). The result of simultaneously inverting both datasets produces better results than either dataset on its own. The amplitude of the anomalies matches the true model better than the inversions from the geophones, while they are better resolved than the inversion from the DAS fibre. This result is not entirely surprising as the inversion is better constrained with additional data, but it motivates the deployment of shaped DAS fibres. It is easier and often cheaper to deploy fibres in horizontal wells than it is to deploy geophones, especially in producing wells. Geophones are better tuned for reflection data than DAS fibres, and are cheaper to deploy for surface acquisition. Simultaneous inversion of geophone and fibre data offers a tangible opportunity for complementary acquisition geometries that lead to more robust inversions.

Inversions for data from the asymmetric fibre presented earlier is shown in figure 14. The quality of the inversion for v_p and v_s is similar to the symmetric helical fibres. The inversion result for density contains a large number of artifacts but is still comparable to quality in the inversions from the helical fibres which all struggled to resolve density, a parameter that is typically difficult to resolve from transmission data.

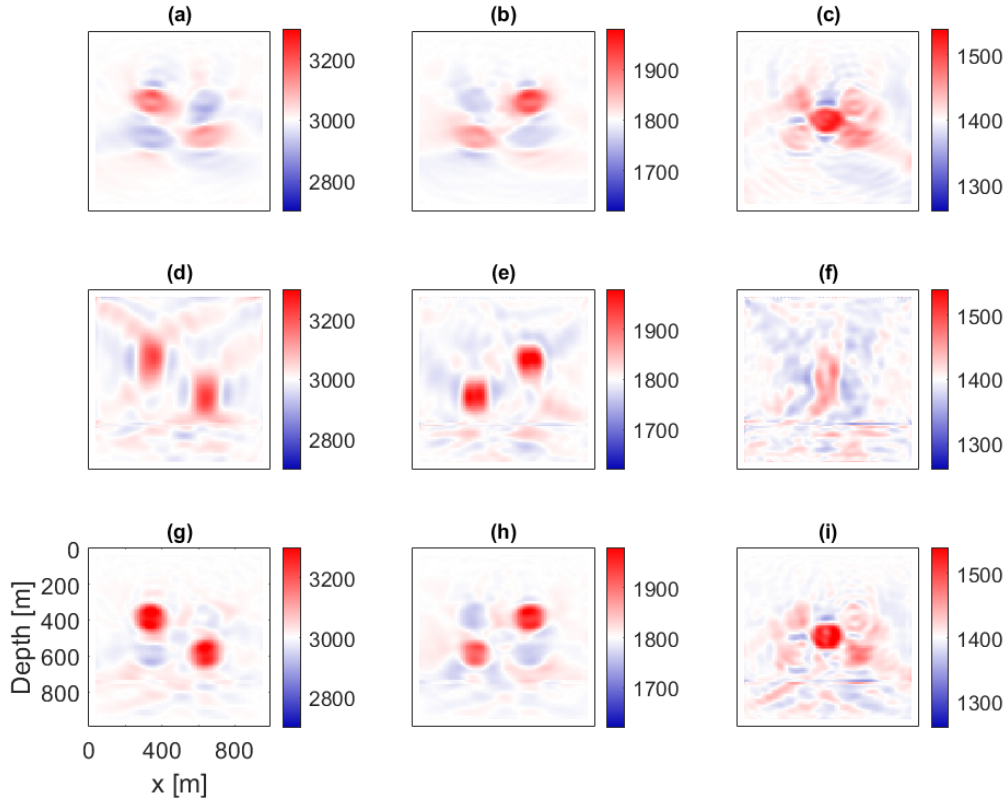


FIG. 13. Inversion results for v_p (column 1), v_s (column 2), and ρ (column 3) for reflection geophone data (a)-(c), strain data from a 1:4 helical fibre in a horizontal well (d)-(f), simultaneous inversion of reflection geophone data and strain data from a 1:4 helical fibre in horizontal well (g)-(i).

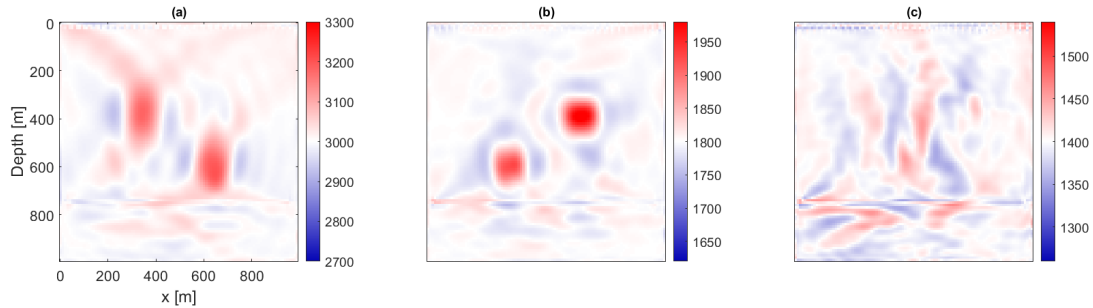


FIG. 14. Inversion results for v_p , v_s and ρ in (a)-(c) respectively for data from a $2\epsilon_{xx} : \epsilon_{xz} : 2\epsilon_{zz}$ asymmetric fibre.

SYNTHETIC EXAMPLE 2: INVERTING FIBRE STRAIN DATA FOR A SECTION OF THE MARMOUSI 2 MODEL

The encouraging results of inverting DAS data from a toy model motivated tests for the inversion of fibre data from a more geologically reasonable model. A portion of the Marmousi2 containing water-wet sand anomalies, a gas charged sand, and a thin oil bearing formation were chosen for this set of examples. Figure 15(a) shows the true density model used for this example, while figure 15(b) shows the extracted sand anomalies. The upper

two anomalies and the far right anomaly represent water-wet sand channels, the middle left anomaly is a gas charged sand, while the thin lower anomaly is an oil bearing sand (Martin et al., 2006). These anomalies are thin and localized, providing a good model for testing the accuracy of simultaneous inversion of DAS and geophone data.

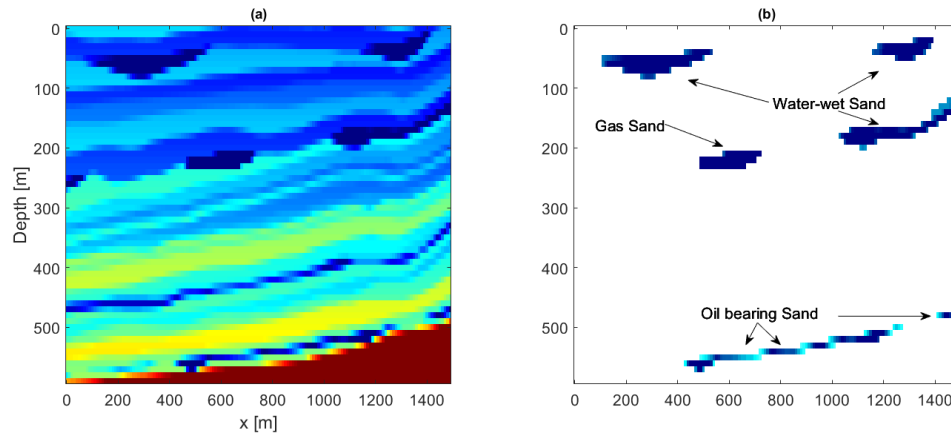


FIG. 15. (a) True density model from a portion of the Marmousi2 model, (b) extracted anomalies of interest.

To test the quality of inversions using DAS data for estimating parameters from a geologic model, an asymmetric fibre similar to the one in figure 4 is placed in the oil bearing formation at the bottom of the model. This simulates a DAS fibre in a horizontal well drilled into a thin oil bearing sand. Data was generated using 30 sources from 20 to 1470 meters with a spacing of 50 meters at a depth of 20 meters. The data from this fibre is inverted for 11 iterations of TGN, with the Hessian being approximated using 25 inner loop iterations of BFGS. The frequency bands consist of 5 evenly spaced frequencies with the first band containing 10-11 Hz data and the final band containing 10-20 Hz data. The high-end of the bandwidth increases by 1 Hz each iteration. Both the 10th and 11th iterations consist of the full bandwidth from 10-20 Hz. The starting models were created through linear gradients of the parameters with depth, ie $v_p(z) = v_{p0} + \alpha * z$. The intercept of these gradients, v_{p0} , v_{s0} , and ρ_0 were calculated by taking the mean value of each parameter within the upper layer. The gradients were chosen to match the slope of the true model, and are 0.5 (m/s)/m, 0.5 (m/s)/m, and 0.2 (kg/m³)/m for v_p , v_s , and ρ respectively.

The results of inverting the DAS data from the fibre in the horizontal well is shown in figure 16. The inversion, using only DAS data, captures the overall trends of the model for v_p and v_s . Specifically, the gas charged channel and oil bearing formation are detected, and the velocity structure with depth is captured. However, the inversions lack resolution, and poorly characterizes the higher frequency structure. This is a result of DAS data from a fibre in the horizontal well recording primarily transmission ray paths, producing data that lacks information about the higher frequency characteristics of the model. However, with only DAS data at transmission angles the major features of the model are characterized. The inversion result for density is less encouraging. While some of the major features of the model are detected, including the gas channel, oil formation, and water-wet sands, the inversion contains inaccuracies. There are regions, especially deeper in the model, where density has increased where it should have decreased. Without access to the true model, it would be challenging to differentiate real structure from errors in the inversion. From the

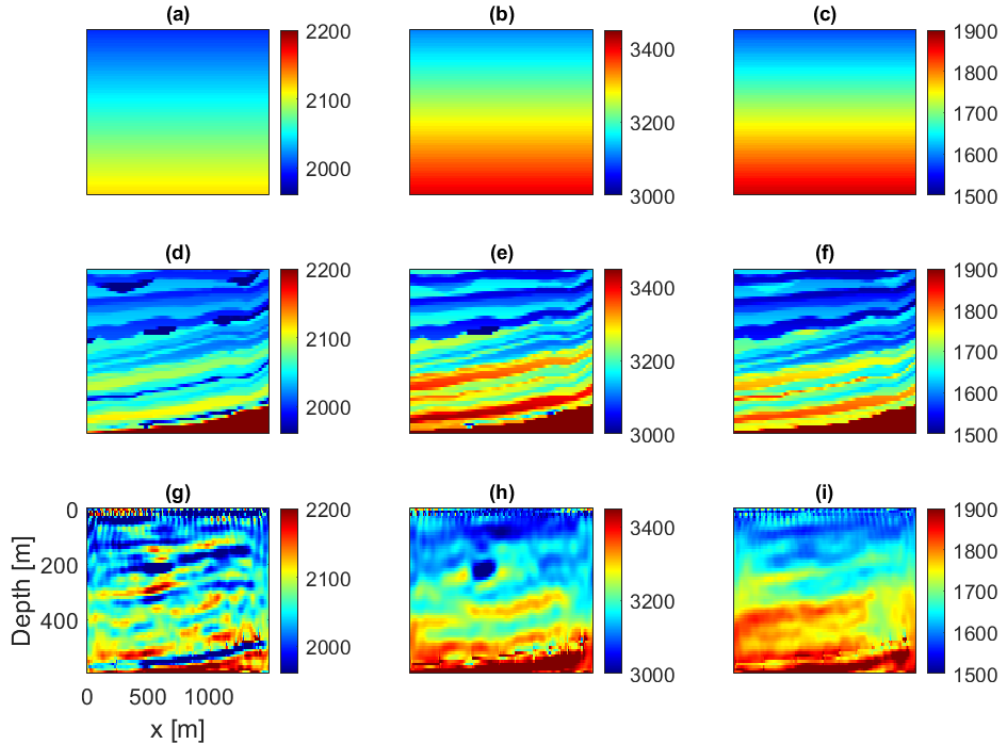


FIG. 16. Starting models for ρ , v_p and v_s in (a)-(c), true models from a section of the Marmoussi 2 model for ρ , v_p and v_s in (d)-(f), and inversion results using a fibre in a horizontal well for ρ , v_p and v_s in (g)-(i).

radiation patterns shown previously, it is evident that significant information about density is contained in the short wavelength reflected waves. It is therefore not surprising that inverting DAS data primarily composed of transmission information struggles to invert for density.

Three profiles were extracted to examine the inversion results in more detail. Figure 17 highlights the location of these profiles. The first was chosen to cross through the far left water-wet sand, 260 meters from the left edge of the model. The second is taken 550 meters from the left edge of the model and passes through the gas charged channel and oil bearing formation. The third passes through the lower water-wet sand and the oil bearing formation, 1100 meters from the left edge of the model. Figure 18 shows the initial (blue dashed line), true (black solid line), and inverted (red dashed line) profiles using DAS data for v_p (column 1), v_s (column 2), and ρ (column 3). These profiles show that inversion with DAS data at transmission angles can recover long wavelength trends in the model, but struggles to recover the high frequency characteristics. While DAS data on its own cannot provide high resolution parameter estimates, this example highlights that it can supply the long wavelength information that reflection data lacks, providing a complementary dataset to geophones.

Surface geophones sample the short wavelength portions of the model, associated with reflection data. When the data lack low frequencies, it can be challenging to recover the

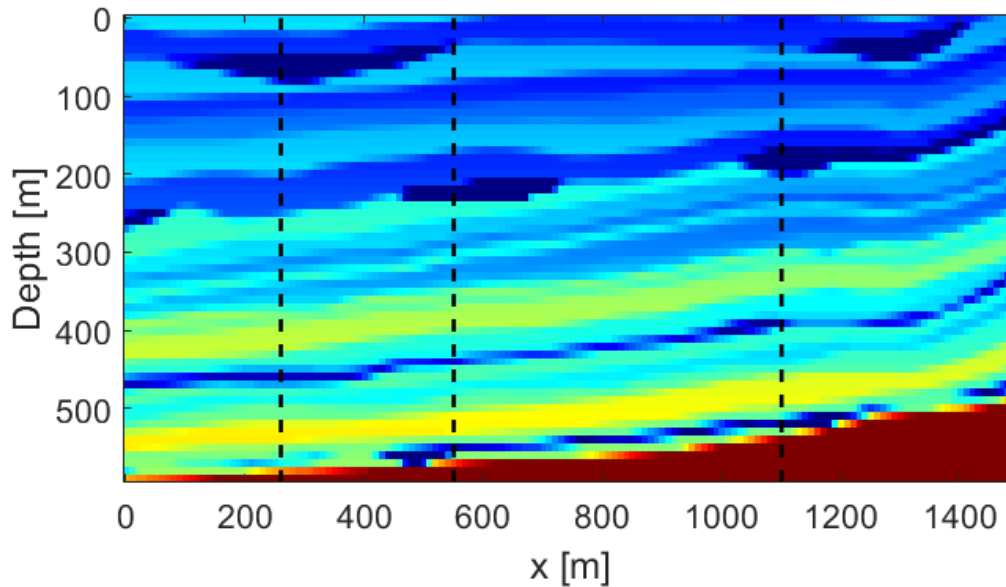


FIG. 17. Marmousi2 density model with locations of the extracted profiles shown by the black dashed lines.

deeper trends in the model using surface geophones alone. Most successful applications of inversion using surface geophone data require very low frequencies. However, when these frequencies are not available it may be necessary to supplement the geophone data with buried DAS fibre, such as that in a horizontal well. To test this idea we perform an inversion of geophone data using the same frequencies as the experiment with only DAS data. We also simultaneously invert the geophone and DAS data together to examine the uplift DAS can provide when low frequencies are missing from the geophone data. The same optimization schedule above is used to invert data from 30 geophones with a spacing of 50 meters at a depth of 20 meters, ranging from 20 meters to 1470 meters from the left edge of the model. Data is also inverted simultaneously from the geophones and DAS fibre. Figure 19 (a)-(c) show the true models, (d)-(f) the inversion from geophone data, and (g)-(i) the inversion for geophone and DAS data for ρ (column 1), v_p (column 2), and v_s (column 3). Figure 20 shows profiles similar to those in figure 18 for the true model (black solid line), inverted models using only geophones (red dashed line), and inverted models using geophones and DAS (blue dashed line).

Figures 19(d)-(f) and 20 (red dashed line) show the results for inverting using only geophone data. It is evident in the inversion for v_p and v_s that the geophones struggle to capture the long wavelength character of the models, especially in the deeper regions. The short wavelength reflection data supplies information about sharp contrasts at interface boundaries. The inversions are able to recover these portions of the model well, but with the missing low frequencies, inversion with geophone data struggle to capture the long wavelength velocity changes within layers. Shallower in the model some of the long wavelength information is provided by diving waves and the inversions are more accurate in these regions. The density inversion matches the true model well, and the important features are well resolved. The inversion for density using only geophone data is more accurate than for velocity due to the majority of information about density being carried by reflected waves.

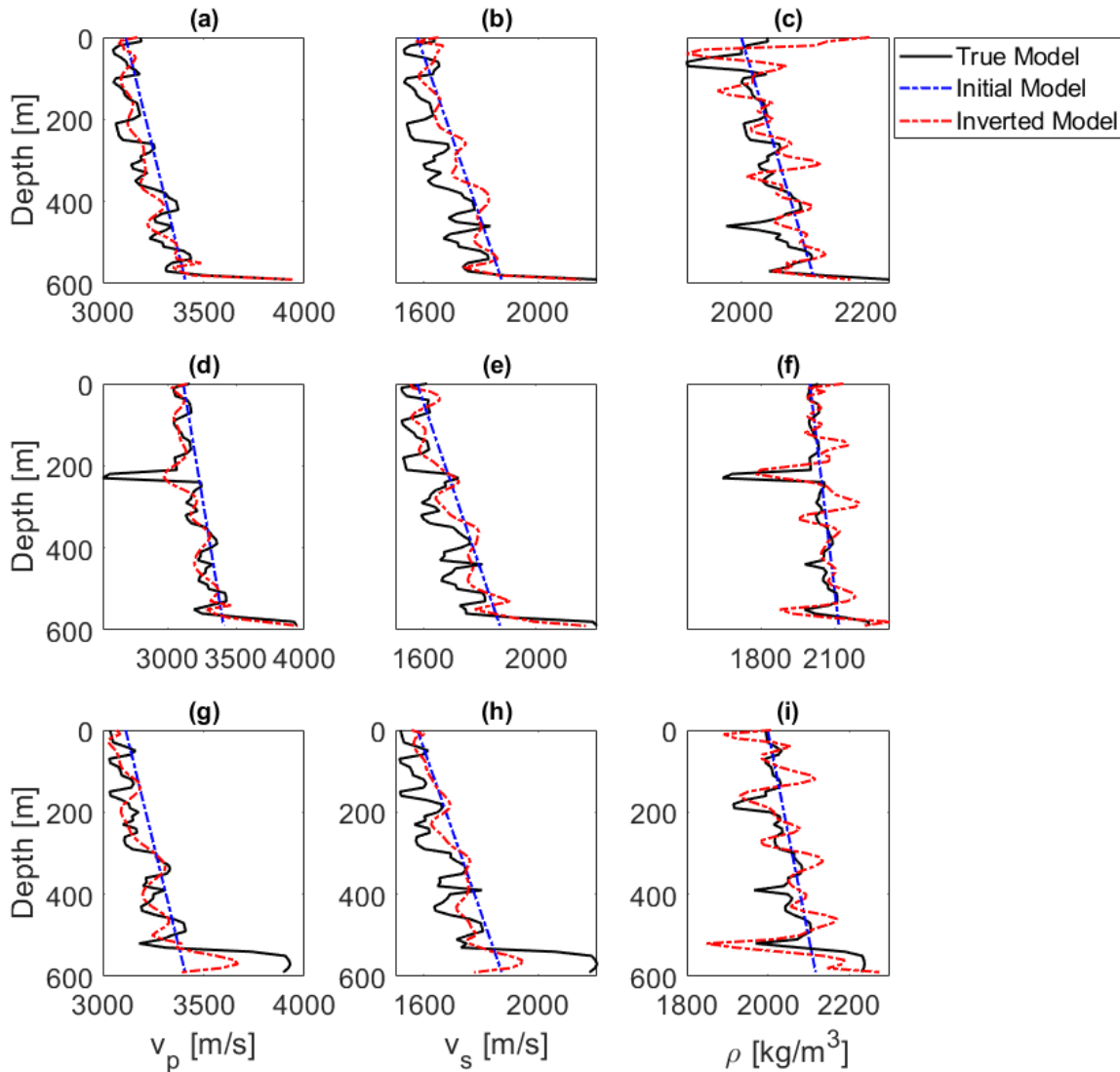


FIG. 18. Profiles extracted from figure 16 for v_p , v_s , and ρ for 260 meters (a)-(c), 550 meters (d)-(f), and 1100 meters (g)-(i) from the left edge of the model. The blue dashed lines indicate the initial model, the black solid lines the true model, and the red dashed lines the inverted model.

The uplift provided by the inclusion of DAS data is evident in figures 19(g)-(i) and 20 (blue dashed line). With the inclusion of DAS data, the long wavelength character of the inverted models is a better match to the true models, especially deeper in the model. Importantly, the character of the oil bearing formation is better resolved with the inclusion of DAS, and the amplitude of the gas channel is a better match to the true model. Density, does not benefit as much from the inclusion of transmission DAS data, but some of the spurious high density errors have been reduced. Both datasets provide complementary information about the model, and the inclusion of both in the inversion provides significant uplift over inverting using either dataset alone.

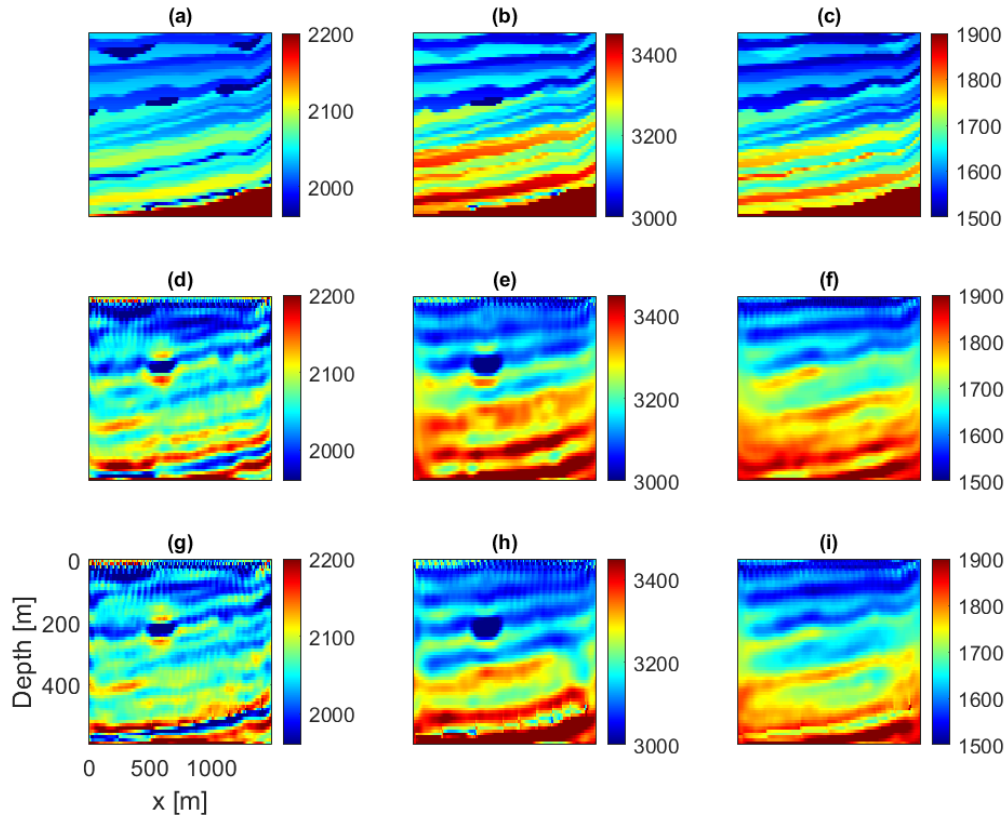


FIG. 19. True models for ρ , v_p and v_s in (a)-(c), inversion results using only geophones for ρ , v_p and v_s in (d)-(f), and inversion results using a fibre in a horizontal well and surface geophones for ρ , v_p and v_s in (g)-(i).

DISCUSSION

The analysis presented here displays the efficacy of using DAS data for high quality parameter estimation using FWI, and presents an opportunity to supplement conventional inversions from geophones alone. Analysis of radiation scattering patterns for v_p , v_s , and ρ for helical and straight DAS fibres revealed the important differences in wavefield information we can record through careful design of fibres geometries. In this paper we looked at symmetric fibres that lack sensitivity to shear strain components (ϵ_{xz}), and presented a special case of a fibre that is blind to shear waves. Fibres that can discriminate between wavefield modes could important implications for future studies. In the clean data case shown here, inverting DAS data for various helical fibres showed that a gentle wind and tight wind did not greatly alter the inversion results. It is hypothesized that the addition of noise will harm the inversions from fibres that are less sensitive in the dominant direction of wavefield propagation due to data deficiency. This is a thread that will be explored in further research.

We also develop a method for the simultaneous inversion of surface geophones and downhole DAS data. Geophones are cheaper to deploy for surface acquisition while DAS fibres can be more readily deployed downhole, especially in producing well, offering com-

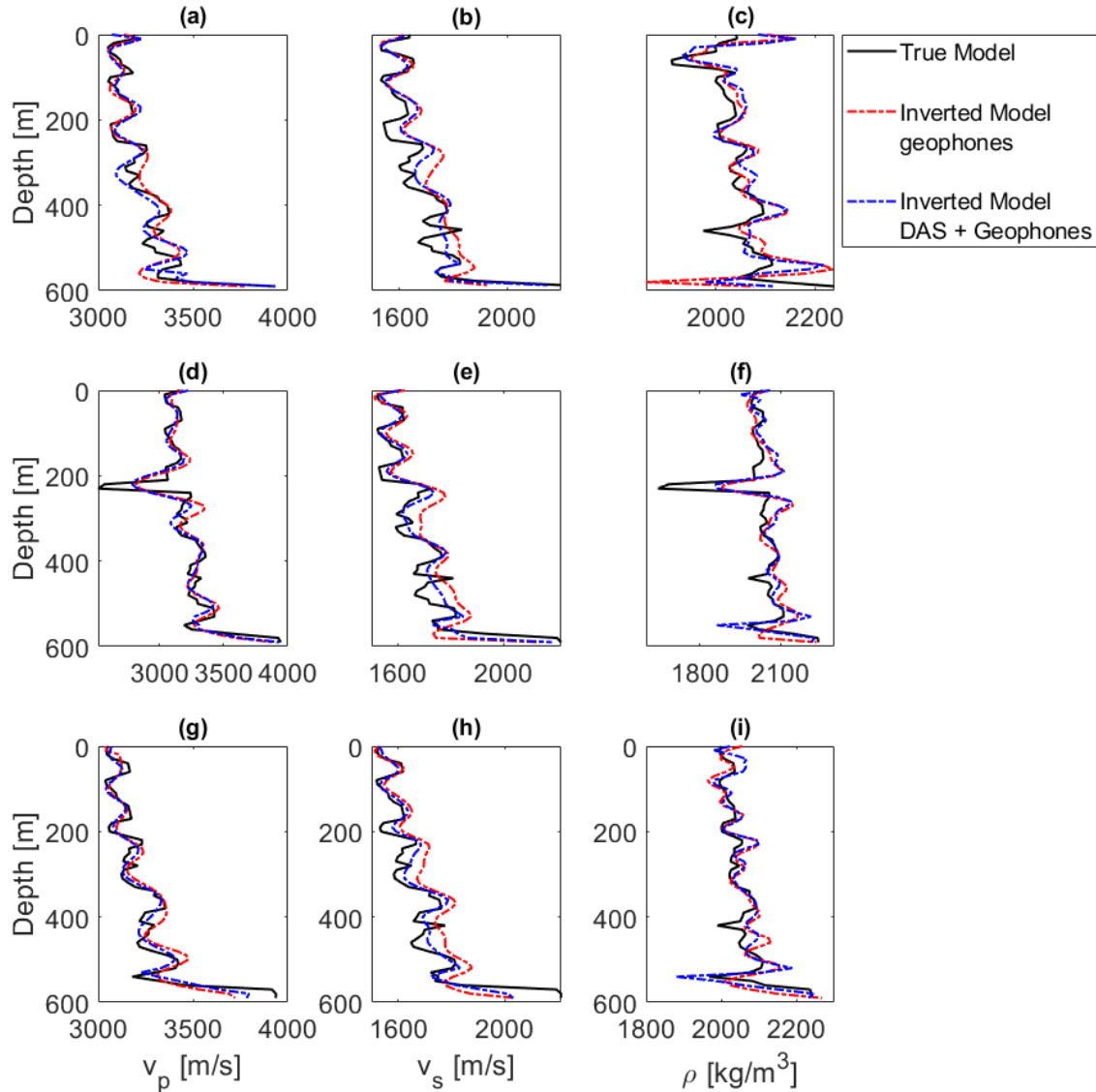


FIG. 20. Profiles extracted from figure 19 for v_p , v_s , and ρ for 260 meters (a)-(c), 550 meters (d)-(f), and 1100 meters (g)-(i). The black solid lines the true model, the blue dashed lines indicate the inverted model using geophones and DAS, and the red dashed lines the inverted model from geophone data alone.

plementary acquisition of data at both reflection and transmission scattering angles. Simultaneous inversion of DAS and geophone data on the toy model provided enhanced parameter estimations. The resulting inversions seems to borrow positive properties from the inversion of the individuals datasets. For example DAS provided a closer match to the amplitudes of the v_p and v_s anomalies at a cost to resolution. The inversion of geophone data provided more resolved estimates, at poorer correlation in amplitude and with larger cross talk artifacts. The combined inversion produced accurate high resolution estimates with reduced cross talk. These results present an opportunity for DAS data to complement geophones in FWI. It was mentioned in the introduction that DAS has a lower frequency floor than geophones, an area of further research is the development of a frequency dependent version of \mathbf{R} that can place stronger emphasis on DAS data at lower frequencies and

include more geophone data as the inversion bandwidth increases.

The results from the toy model encouraged further investigation of the efficacy of inverting DAS data on a more complex geologic model. A section of the Marmousi2 containing thin hydrocarbon formations and localized channels deposits was inverted with a DAS fibre in a horizontal well. The resulting parameter estimates recovered the long wavelength components of the true model, highlighting the ability of DAS data to supply long wavelength parameter estimates. Including geophone data with DAS data greatly improved the results over using either dataset alone. As the use of DAS continues to expand it is important to develop frameworks to leverage it in parameter estimations and this study offers insights into the ability of DAS to supply high resolution models.

CONCLUSIONS

In this study we develop a method for inverting DAS strain data from fibres of arbitrary geometric complexity, by expanding the reach of conventional FWI algorithms. By analyzing the sensitivity of fibre geometries to scattering radiation patterns, we have also provided a tool for survey design in which we can choose the best fibre for a given purpose prior to deploying it downhole. Our method offers the ability to simultaneously invert DAS strain data and 3C geophone data providing very high resolution parameter estimates. A toy model was inverted using four helical fibre geometries with varying lead angles, and the effect of the lead angle on inversion results was investigated. This model was also inverted using a simultaneous inversion of surface geophone and downhole DAS data providing improved parameter estimates over inverting either dataset alone. A section of the Marmousi2 model was inverted by using DAS data from horizontal well tracking an oil bearing formation. The result presented here prove the efficacy of DAS data in providing high resolution parameter estimates and solidify a place for DAS within FWI. An interesting secondary development of this study was the realization of fibre geometry that is blind to shear wave modes, opening the door for research into fibre geometries that can discriminate against other wave modes, potentially leading to fibres tuned for p-waves, s-waves, and surface waves.

ACKNOWLEDGMENTS

The authors would like to thank the sponsors of the CREWES project as well NSERC under the grant CRDPJ 461179-13 for making this work possible through their financial support. Matt Eaid and Scott Keating were partially supported through scholarships from the SEG foundation.

REFERENCES

- Becker, M., and Coleman, T., 2019, Distributed acoustic sensing of strain at Earth tide frequencies: *Sensors*, **19**.
- Becker, M. W., Ciervo, C., Coleman, T., and Mondanos, M., 2018, Fracture hydromechanical response measured by distributed acoustic sensing at millihertz frequencies: *Geophysical Research Letters*, **44**, No. 14, 7295–7302.
- Brossier, R., Operto, S., and Virieux, J., 2009, Seismic imaging of complex onshore structures by 2d elastic frequency-domain full-waveform inversion: *Geophysics*, **74**, No. 6.

- Bunks, C., 1995, Multiscale seismic waveform inversion: *Geophysics*, **60**, No. 5.
- Daley, T., Freifeld, B., Ajo-Franklin, J., Dou, S., Pevzner, R., Shulakova, V., Kashiakr, S., Miller, D., Goetz, J., Hennings, J., and Lueth, S., 2013, Field testing of fiber-optic distributed acoustic sensing (DAS) for subsurface seismic monitoring: *The Leading Edge*, **32**, No. 6, 593–724.
- Dou, S., Ajo-Franklin, J., Daley, T., Robertson, M., Wood, T., Freifeld, B., Pevzner, R., Correa, J., Tertyshnikov, K., Urosevic, M., and Gurevich, B., 2016, Surface orbital vibrator (SOV) and fiber-optic DAS: Field demonstration of economical, continuous-land seismic time-lapse monitoring from the Australian CO2CRC Otway site: SEG Expanded Abstracts.
- Dou, S., Lindsey, N., Wagner, A., Daley, T., Freifeld, B., Robertson, M., Peterson, J., Ulrich, C., Martin, E., and Ajo-Franklin, J., 2017, Distributed acoustic sensing for seismic monitoring of the near surface: A traffic-noise interferometry case study: *Scientific Reports*, **7**, No. 11620.
- Eaid, M., Li, J., and Innanen, K., 2018, Modeling the response of shaped-DAS fibres to microseismic moment tensor sources: SEG Expanded Abstracts.
- Egorov, A., Correa, J., Bona, A., Pevzner, R., Tertyshnikov, K., Glubokovskikh, S., Puzyrev, V., and Gurevich, B., 2018, Elastic full-waveform inversion of vertical seismic profile data acquired with distributed acoustic sensors.: *Geophysics*, **83**, No. 3, 1MJ–Z13.
- Innanen, K., 2017, Determination of seismic tensor strain from HWC-DAS cable with arbitrary and nested-helix winds: SEG Expanded Abstracts.
- Jin, G., and Roy, B., 2017, Hydraulic-fracture geometry characterization using low-frequency DAS signal: *The Leading Edge*, **36**, No. 12, 962–1044.
- Karam, S., Webster, P., Hornman, K., Lumens, P., Franzen, A., Kindy, F., Chiali, M., and Busaidi, S., 2013, Microseismic applications with DAS: 4th EAGE Passive Seismic Workshop.
- Karrenbach, M., Cole, S., Ridge, A., Boone, K., Kahn, D., Rich, J., Silver, K., and Langton, D., 2018, Fiber-optic distributed acoustic sensing of microseismicity, strain and temperature during hydraulic fracturing: *Geophysics*, **84**, No. 4, D11–D23.
- Krebes, S., 2019, *Seismic Wave Theory*: Cambridge University Press, 1 edn.
- Kuvshinov, B. N., 2015, Interaction of helically wound fibre-optic cables with plane seismic waves: *Geophysical Prospecting*, **64**, No. 3.
- Luo, S., and Sava, P., 2011, A deconvolution-based objective function for wave-equation inversion: SEG Expanded Abstracts 81 International Meeting.
- Martin, G., Wiley, R., and Marfurt, K., 2006, Marmousi2: An elastic upgrade for Marmousi: *The Leading Edge*, **25**, 156–166.
- Masoudi, A., Belal, M., and Newson, T., 2013, A distributed optical fibre dynamic strain sensor based on phase-OTDR: *Measurement Science and Technology*, **24**.
- Mateeva, A., Lopez, J., Potters, H., Mestayer, J., Cox, B., Kiyashchenko, D., Wills, P., Grandi, S., Hornman, K., Kuvshinov, B., Berlang, W., Yang, Z., and Detomo, R., 2014, Distributed acoustic sensing for reservoir monitoring with vertical seismic profiling: *Geophysical Prospecting*, **62**, No. 4, 679–692.
- Mestayer, J., Karam, S., Cox, B., Wills, P., Mateeva, A., Lopez, J., Hill, D., and Lewis, A., 2012, Distributed acoustic sensing for geophysical monitoring: 74th EAGE Conference and Exhibition.
- Metivier, L., Allain, A., Brossier, R., Merigot, Q., Oudet, E., and Virieux, J., 2018, Optimal transport for mitigating cycle skipping in full-waveform inversion: A graph-space transform approach: *Geophysics*, **83**, No. 5, R515–R540.
- Metivier, L., Brossier, R., Virieux, J., and Operto, S., 2013, Full waveform inversion and the truncated newton method: *Siam J. Sci. Comput.*, **35**, B401–B437.

- Ning, I., and Sava, P., 2018, Multicomponent distributed acoustic sensing: Concept and theory: *Geophysics*, **83**, No. 2.
- Nocedal, J., and Wright, S. J., 2006, *Numerical Optimization*: Springer, 2 edn.
- Podgornova, O., Leaney, S., Zeroug, S., and Liang, L., 2017, On full-waveform modeling and inversion of fiber-optic VSP data: SEG Expanded Abstracts.
- Posey Jr., R., Johnson, G., and Vohra, S., 2000, Strain sensing based on coherent Rayleigh scattering in an optical fibre: *IEE Electronics Letters*, **36**, No. 20.
- Pratt, R., 1990, Frequency-domain elastic wave modeling by finite differences: A tool for crosshole seismic imaging: *Geophysics*, **55**, No. 5, 514–639.
- Pressley, A., 2012, *Elementary Differential Geometry*: Springer, 2 edn.
- Tarantola, A., 1984, Inversion of seismic reflection data in the acoustic approximation: *Geophysics*, **49**.
- Tarantola, A., 1986, A strategy for nonlinear elastic inversion of seismic reflection data: *Geophysics*, **51**, 1893–1903.
- Tarantola, A., 1988, Theoretical background for the inversion of seismic waveforms, including elasticity and attenuation: *Pure and Applied Geophysics*, **128**, No. 1/2, 365–399.
- Todd, M., Johnson, G., and Chang, C., 1999, Passive, light intensity-independent interferometric method for fibre Bragg grating interrogation: *IEE Electronics Letters*, **35**, No. 22.
- van Leeuwen, T., and Mulder, W., 2010, A correlation-based misfit criterion for wave-equation travel time tomography: *Geophysics Journal International*.
- Virieux, J., and Operto, S., 2009, An overview of full-waveform inversion in exploration geophysics: *Geophysics*, **74**, No. 6, WCC127–WCC152.
- Warner, M., and Guasch, L., 2016, Adaptive waveform inversion: theory: *Geophysics*, **74**, No. 6.